Biomaterials Advances 150 (2023) 213426

Contents lists available at ScienceDirect

Biomaterials Advances

journal homepage: www.journals.elsevier.com/materials-science-and-engineering-c

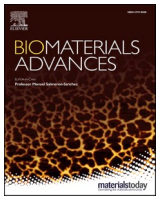

# 3D bioprinted functional skeletal muscle models have potential applications for studies of muscle wasting in cancer cachexia

Andrea García-Lizarribar [a,b], Aranzazu Villasante [a,c,*], Jose Antonio Lopez-Martin [d,e], Marta Flandez [d], M. Carmen Soler-Vázquez [f], Dolors Serra [f,g], Laura Herrero [f,g], Ana Sagrera [h], Alejo Efeyan [h], Josep Samitier [a,b,c,*]

[a] Institute for Bioengineering of Catalonia Barcelona Institute of Science (IBEC-BIST), 08028 Barcelona, Spain
[b] Centro de Investigación Biomédica en Red (CIBER-BBN), 28029 Madrid, Spain
[c] Department of Electronic and Biomedical Engineering, University of Barcelona (UB), 08028 Barcelona, Spain
[d] Clinical & Translational Cancer Research Group, Instituto de Investigación Sanitaria Hospital 12 de Octubre (i+12), Av Córdoba s/n, 28041 Madrid, Spain
[e] Medical Oncology Department, Hospital Universitario 12 de Octubre, Av de Córdoba s/n, 28041 Madrid, Spain
[f] Department of Biochemistry and Physiology, School of Pharmacy and Food Sciences, Institut de Biomedicina de la Universitat de Barcelona (IBUB), UB, Spain
[g] Centro de Investigación Biomédica en Red de Fisiopatología de la Obesidad y la Nutrición (CIBEROBN), Instituto de Salud Carlos III, Madrid, Spain
[h] Metabolism and Cell Signaling Laboratory, Spanish National Cancer Research Centre (CNIO), Madrid, Spain

ARTICLE INFO

*Keywords:*
Bioprinting
Skeletal muscle
Cachexia
Tissue-engineering

ABSTRACT

Acquired muscle diseases such as cancer cachexia are responsible for the poor prognosis of many patients suffering from cancer. *In vitro* models are needed to study the underlying mechanisms of those pathologies. Extrusion bioprinting is an emerging tool to emulate the aligned architecture of fibers while implementing additive manufacturing techniques in tissue engineering. However, designing bioinks that reconcile the rheological needs of bioprinting and the biological requirements of muscle tissue is a challenging matter. Here we formulate a biomaterial with dual crosslinking to modulate the physical properties of bioprinted models. We design 3D bioprinted muscle models that resemble the mechanical properties of native tissue and show improved proliferation and high maturation of differentiated myotubes suggesting that the GelMA-AlgMA-Fibrin biomaterial possesses myogenic properties. The electrical stimulation of the 3D model confirmed the contractile capability of the tissue and enhanced the formation of sarcomeres. Regarding the functionality of the models, they served as platforms to recapitulate skeletal muscle diseases such as muscle wasting produced by cancer cachexia. The genetic expression of 3D models demonstrated a better resemblance to the muscular biopsies of cachectic mouse models. Altogether, this biomaterial is aimed to fabricate manipulable skeletal muscle *in vitro* models in a non-costly, fast and feasible manner.

## 1. Introduction

During skeletal muscle development and tissue regeneration, muscle precursor cells (myoblasts) fuse to produce multi-nucleated myotubes that will further differentiate to form myofibers [1]. This process is accompanied by an equilibrated synthesis, degradation and rearrangement of numerous proteins that ensure the alignment of muscle fibers, formation of sarcomeres and muscle contraction.

Acquired muscle diseases are characterized by a dramatic loss of muscle mass, which has been associated with an unbalanced protein turnover. The severe and progressive muscle atrophy ends in a significant loss of body mass called cachexia, which is responsible for 20 % of death in cancer patients [2]. Cancer cachexia (CC) is a multifactorial syndrome characterized by systemic inflammation, uncontrolled weight loss and dramatic metabolic alterations [3]. The mechanism of CC is not well understood and there are no specific treatments for this disease. Muscle tissue samples from patients are obtained by invasive methods such as biopsies, which have limited lifespan and size. Instead, tissue-engineering approaches can mimic *in vitro* the native skeletal muscle features for treating traumatic injuries or degenerative diseases, but also

* Corresponding authors at: Institute for Bioengineering of Catalonia (IBEC), The Barcelona Institute of Science and Technology (BIST), C/ Baldiri Reixac 15-21, 08028 Barcelona, Spain.
*E-mail addresses:* avillasante@ibecbarcelona.eu (A. Villasante), jsamitier@ibecbarcelona.eu (J. Samitier).

https://doi.org/10.1016/j.bioadv.2023.213426
Received 4 October 2022; Received in revised form 1 April 2023; Accepted 8 April 2023
Available online 19 April 2023

are being used as predictive models of diseases for drug screenings [4].

Currently, *in vitro* studies of cachexia are based on monolayer cultures with medium conditioned with cancer cell lines supernatant [5–7], 3D organoids/spheroids [7] of cancer cells and high concentration of glucocorticoids [8,9] or inflammatory cytokines [10] to upregulate the expression of atrophy related genes. However, there is a clear need to find *in vitro* models that replicate the physiological conditions of healthy and diseased skeletal muscle more accurately to obtain reliable preclinical outcomes.

The gold standard strategy for engineering skeletal muscle is currently based on the combination of myogenic cells and biomaterials to resemble the muscle architecture, matrix composition and and mechanical properties. The physical constraints of such biomaterials must ensure cell-cell contact events to favor cell fusion and, and muscle fiber alignment, which is essential for muscle functionality [11–13].

In the last decades, the fibrous architecture of skeletal muscle has been replicated using hydrogel-based technologies. Fiber-shaped 3D cultures are produced using micromolding and extrusion-based methods, such as 3D bioprinting. Micromolding is based on the use of non-degradable molds where cell-laden hydrogels are poured to assume the negative shape [14]. Mature and electrically responsive muscle fibers were achieved using type I collagen [15], fibrin [13,16] and matrigel [17]. Differentiated myotubes were aligned using either channel-shaped molds [13,16] or helped by the passive tension forces of two opposite pillars [17]. Micromolding is simple, cost-effective and reproducible, however, it suffers from low scalability, limited recapitulation of native architectures, time-consuming manufacturing and lack of vascularization.

Recently, 3-dimensional (3D) bioprinting has emerged as an alternative to traditional technologies for fiber alignment. Several studies demonstrated that shear stress of the extrusion printing needle aligned biomaterial fibers towards the printing direction, which was of great interest in developing aligned muscle fibers [18,19]. This technology allows the controlled delivery of biomaterials loaded with cells or therapeutic factors in a spatially defined manner to produce clinically relevant size models, thus opening up the possibility of *in situ* bioprinting approaches for personalized medicine or the automated fabrication of *in vitro* models.

Shape fidelity of printed constructs is strongly dependant on the physical properties of biomaterials, and is achieved using indirect bioprinting, microfluidic assisted bioprinting or direct bioprinting [20]. The main strategy of indirect and microfluidic assisted bioprinting is the use of sacrificial or supporting materials that work as a permanent or transitory printed micromolds to provide cylindrical shape to the cell-ladden biomaterials. Those techniques are particularly useful with low viscous solutions as collagen [21], Matrigel [22] fibrin [23], and, which show excellent myogenic properties. Skeletal muscle models with highly mature and functional fibers were built with Matrigel using a microvalve-based drop-on-demand technique (DOD) bioprinting system [22]. Due to the low viscosity and expansion of printed Matrigel, muscle fibers are aligned through tension forces using opposite posts. Another strategy to retain the shape of extruded fibers and align muscle cells is based on mixtures with high viscous materials as gelatin [23]. Those materials are crosslinked in downstream processes and need further steps to remove sacrificial material, which lengthens the production time.

Direct bioprinting is based on the deposition of self-standing strands using highly viscous materials that preserve the shape of the extruded filament. O'Conell et al. [24] proposed a protocol to define highly printable bioinks. First, only bioinks that exhibit string morphology when extruded should be considered for subsequent printability test. Second, two printed and crossed lines must stack atop one another and avoid merging. Daly et al. [25] assessed bioink printability by calculating the spreading ratio, which was defined as the width of the printed filament divided by the needle diameter. They described highly printable bioinks as those with a spreading ratio lower than 2.5. Crosslinking steps after printing can be dismissed using photocrosslinkable materials. Gelatin methacryloyl (GelMA) is highly printable, with versatile mechanical properties and can be combined with complementary materials to mimic the physical and biological properties of native skeletal muscle [26]. So far, the main limitation of 3D bioprinting is the development of myogenic biomaterials, since highly printable materials often present cell viability constraints, mainly due to the limited porosity [27,28]. Indeed, most current models produced by direct 3D bioprinting do not show *in vitro* contractile activity [29–31].

We previously reported composite bioinks based on GelMA that supported the myogenic differentiation [32]. We verified that extrusion bioprinting can align the encapsulated cells in the printed filament. However, the limited porosity and nutrient diffusion hampered the proliferation and differentiation of muscle fibers within the core of 3D cultures. There is a clear need to optimize the formulation of bioinks for the production of high-throughput muscle *in vitro* models with an excellent microenvironment for the proliferation and differentiation of functional muscle fibers using direct 3D bioprinting.

This study develops myogenic bioinks that mimic the native tissue to produce scalable 3D skeletal muscle models by direct 3D bioprinting that serve as contractile *in vitro* platforms. We tune the crosslinked hydrogels' physical properties to improve myoblasts' proliferation and differentiation into mature myofibers using mouse and human myoblasts. The model's versatility allows its adaptation to different platforms, such as an electrical pulse stimulation system and a Seahorse platform for the life-monitoring of muscle functionality. Using the developed 3D bioprinted models of muscle wasting we obtain similar genotypic features when we compare with mice quadriceps muscles affected by cancer cachexia. Based on this best resemblance, for the first time, we propose using a bioprinted muscle to recapitulate, at least in part, cancer cachexia *in vitro*. We confirmed that the engineered muscle is a feasible tool for further studies of biological mechanisms and drug responses of skeletal muscle wasting produced by cancer cachexia.

## 2. Materials and methods

### 2.1. Chemical modification of natural polymers

Gelatin from porcine skin and sodium alginate were methacrylated as described in previous work [32]. Briefly, gelatin (10 % *w/v*) was dissolved in DPBS 1× at 50 °C and reacted 1 h with methacrylic anhydride (1.25 % *v/v*) at constant stirring. The reaction was stopped with an excess of DPBS 1×. Alginate (1 %) was dissolved in MES buffer at 40 °C. EDC and NHS were added to the solution and reacted overnight with AEMA (0.38 % *w/v*) at constant stirring. AlgMA was precipitated with acetone and filtered. AlgMA was reconstituted with deionized water (1 % *w/v*). Both GelMA and AlgMA were dialyzed against deionized water to remove the unreacted methacrylate for 3 days. They were freeze-dried and stored at −20 °C.

### 2.2. Biomaterial mixtures preparation

GelMA (5 % w/v) and AlgMA (1 % *w/v*) were sterilized with UV light and dissolved in the corresponding growth medium at 40 °C. Lithium phenyl-2,4,6-trimethyl-benzoyl phosphinate (LAP) photoinitiator (TCI Ltd., Tokyo) stock solutions were prepared in a growth medium and added to final concentrations of 0.05 %, 0.02 %, and 0.01 % in w/v%. In those samples containing fibrin, 5 mg/ml of fibrinogen from bovine plasma was added to the mixture and crosslinked with 0.25UI/ml of thrombin from bovine plasma. All reagents were purchased from Sigma-Aldrich unless specified.

### 2.3. Cell culture

C2C12 myoblasts were purchased from ATCC. They were cultured in growth medium (GM) based on DMEM high glucose with L-glutamine

supplemented with FBS (10 % *v*/v), penicillin/streptomycin (1 % v/v), and sodium pyruvate (1 % v/v) at 37 °C with 5 % $CO_2$. For differentiation experiments in 2D cultures, medium was switched to DMEM supplemented with calf serum (2 % v/v), HEPES buffer (2 % v/v), penicillin/streptomycin (1 % v/v) and L-glutamine (1 % v/v), named as DM. Human skeletal muscle myoblasts (HSMM) were purchased from Lonza (Switzerland). They were cultured in SkBM™-2 basal medium (Lonza) supplemented with SkGM™-2 SingleQuots™ Supplement Pack (Lonza). For differentiation in 2D cultures, the medium was switched to SkBM™-2 basal medium supplemented with horse serum (2 % *v*/v) and penicillin/streptomycin (1 % *v*/v). For differentiation in 3D cultures, C2C12 and HSMM were maintained in complete growth mediums unless specified otherwise.

For cachexia experiments, LS174T (human colon cancer cell line) was purchased from ATCC and cultured in EMEM supplemented with FBS (10 % *v*/v) and penicillin/streptomycin (1 % v/v). HCT116 human colon cancer cell line was kindly provided by Dr. Manuel Serrano (IRB, Barcelona. Spain) and cultured in DMEM high glucose with L-glutamine supplemented with FBS (10 % v/v) and penicillin/streptomycin (1 % v/v). Both cell lines were expanded to 80 % confluency. Then, the medium was changed to C2C12 GM, and cells were incubated for 48 h. The medium was collected and centrifuged for 10 min at maximum rpm. The resulting supernatant was stored at −20 °C and used as a conditioned medium (CM).

### 2.4. Bioprinting of muscle rings

C2C12 or HSMM were embedded in GelMA-AlgMA-Fib pre-gels to a final density of $10 \cdot 10^6$ cells/ml and $15 \cdot 10^6$ cels/ml respectively. Bioinks were loaded in 3 cc bioprinting syringes (Nordson, USA) and placed in the extrusion head of the 3D Discovery bioprinter (RegenHU, Switzerland). Ring-shaped models of 4.5 mm diameter and 5 layers were designed with BioCAD software. Rings were printed using 200 μm inner diameter tips (Nordson) at 2 bars pressure, 18 °C, and 2 mm/s printing rate. Each layer was photocrosslinked for 4 s of UV light. Crosslinked rings were immediately submerged in the growth medium free of molds and changed after 24 h to remove the unreacted products. The medium was changed daily while rings were contracted due to cell activity.

### 2.5. Electric stimulation system

Muscle rings were anchored in bioprinted silicon pillars. DOWSIL™ 1700 Clear W/C (DOW Inc., USA) silicon was prepared and loaded into 3 cc bioprinting syringes to fabricate the pillars. The simulation platform was composed of 4 pillars aligned on the vertical axis of each well of a 6-well cell culture plate (Thermofisher). Pillars of 5 × 1 mm and 5 layers were printed at equal intervals in 24 × 24 mm glass slides with 580 μm tips, 2 bar pressure, and 2 mm/s printing rate at room temperature. Coverslips with pillars were crosslinked overnight at 60 °C and then placed into 6-well plates. Differentiated muscle rings were fit and immobilized in the pillars. C-dish covers (IonOptix, USA) were used for electric stimulation. C-dish was connected to an LPA05 amplifier (N4L, UK) that received the signal from the WW5061 waveform generator (Tabor Electronics, Israel). Signal was monitored with DSO3062A Oscilloscope (Agilent Technologies, USA). Muscle rings were stimulated for 1 h during 3 consecutive days with 20 V, 1 Hz, and 2 ms biphasic square pulse. Contraction amplitude of printed muscle was measured from video recordings using MUSCLEMOTION open-source software [33].

### 2.6. Biomaterial characterization

#### 2.6.1. Swelling

Biomaterial disks were weighted before immersion in deionized water ($W_0$). Then, disks were weighted after 15, 30, 60, 120, 180, 240, and 300 min of immersion ($W_N$). Swelling curves were calculated using the following formula: $Swelling\ (\%) = \frac{W_N - W_0}{W_N} \cdot 100$. Maximum swelling was calculated as the average of swelling values on the plateau region of the swelling curves.

#### 2.6.2. Porosity and SEM images

Overall porosity was calculated as the percentage of macropore volume over the total volume of the disk, using the formula: $Porosity\ (\%) = \frac{\frac{W_S - W_D}{\rho_{H_2O}}}{\pi \cdot d^2 \cdot h} \cdot 100$. Where $W_S$ is the weight of the disk at maximum swelling and $W_D$ is the weight of the disk after the removal of the water in macropores. SEM images were acquired as follows to confirm the porosity results. Swelled disks were dehydrated with a serial increase of ethanol solutions. Ethanol was replaced by liquid $CO_2$ and by slowly heating. $CO_2$ achieved gas phase equilibrium at 35 °C and 85.06 atm and was slowly drained. After critical point drying, hydrogels were imaged by ultrahigh-resolution scanning electron microscopy (Nova NanoSEM 230, FEI Company, The Netherlands) operating in low vacuum mode (0.5 mbar of water vapor pressure).

#### 2.6.3. Degradation

To estimate the enzymatic degradation of muscle ECM during development in an accelerated manner, hydrogels were exposed to collagenase IV (Thermofisher). 6 mm diameter disks were incubated with 10 UI/ml of the enzyme. The degradation index was calculated as the slope of the degradation curves obtained with the following formula: $ass\ loss = 1 - \frac{W_N}{W_0}$, where $W_N$ is the weight of the disk at $t_N$, and $W_0$ is the weight of the disk at $t_0$.

#### 2.6.4. Stiffness

The Young's Modulus of the biomaterial mixtures was calculated from the uniaxial compression of swelled disks in a 5 N load cell of Zwick Z0.5 TN instrument (Zwick-Roell, Germany). Samples were tested at room temperature up to 30 % final strain (deformation), using the following parameters: 0.1 mN preload force and 20 %/min strain rate. Stress-strain curves were obtained from load-deformation measurements. Values for the compressive modulus were calculated from the slope of the linear region corresponding to 10–20 % strain.

### 2.7. Myoblast viability and proliferation within biomaterials

Bioprinted muscle rings were cultured for 3 days and stained for 30 min at 37 °C with LIVE/DEAD® Viability/Cytotoxicity Kit for mammalian cells (Thermofisher). Rings were washed twice with DPBS 1×, and images were immediately acquired with LSM 800 confocal microscope (Zeiss, Germany). Live and dead cell percentages from 400 μm width stacks were calculated using FIJI free software (http://rsb.info.nih.gov/ij, National Institutes of Health, USA). Live/Dead images were used to study the morphology of the cells and determine the adhesion to the biomaterials. Cell contour was thresholded, and circularity degree was calculated with particle analyzer macro of FIJI. Frequency distribution histograms were generated with Prism (GraphPad Software Inc., USA).

Quant-iT PicoGreen® dsDNA kit reagent (Thermofisher) was used to determine myoblast proliferation following the manufacturer's protocol. The μg/ml of DNA of a known number of myoblasts was calculated to obtain the number of cells per ml. Samples were normalized by the ring weight, and proliferation was represented as the number of cells per gram of biomaterial to avoid the effect of the ring size variability.

### 2.8. Immunostaining of differentiated fibers

Bioprinted muscle rings were differentiated for 13 days in culture. Rings were fixed for 30 min with 4 % formaldehyde solution in DPBS 1×, followed by blocking and permeabilization in FBS (10 % *v*/v), BSA (2 % *w*/*v*), and Triton X-100 for 1 h. Myosin heavy chain and α-actinin were

stained with MF20 (1:500, Thermofisher) and ACTN2 (1:250, Thermofisher) primary antibodies in 1:1 DPBS1X and blocking-permeabilizing solution overnight at 4 °C. Primary antibodies were conjugated with Alexa Fluor donkey anti-mouse 568 (1:100, Thermofisher) and Alexa Fluor goat anti-rabbit 647 (1:500, Thermofisher) in 1:1 DPBS1X and blocking-permeabilizing solution overnight at 4 °C. Subsequently, samples were stained with Cytopainter Phalloidin-ifluor 488 (1:1000, Abcam, UK) and Hoescht 33,342 (1:1000, Thermofisher) for 1.5 h at room temperature, followed by 3 washing steps in DPBS1X. Fluorescence images were acquired with a confocal microscope. F-actin coverage was calculated with FIJI. MHC staining was quantified to calculate the fusion index and fiber width of electrically stimulated models. Fusion index was calculated as the number of nuclei inside MHC-positive fibers over the total number if nuclei (Supplementary Fig. 4).

For paraffined sections, rings were fixed in 4 % formaldehyde for 45 min and embedded in paraffin. Rings were deparaffined and antigen retrieval was performed in citrate buffer. Afterwards, samples were permeabilized in 0.5 % Triton X-100 for 2 h and blocked in 2 % BSA for 2 h at RT. Slides were then incubated overnight at 4 °C in anti-Phospho-S6 Ribosomal Protein (Ser235/236) 1:200 (CST, USA). Finally, slides were stained with Alexa-Fluor goat anti-rabbit 1:300 for 2 h at RT and with DAPI 1:5000 for 20 min at RT.

### 2.9. Gene expression

2D and 3D cultures, samples were mechanically homogenized in TRIzol™ Reagent (Thermofisher), and RNA was extracted following the manufacturer's protocol; cDNA retrotranscription was obtained using Ready-To-Go You-Prime First-Strand Beads (GE Healthcare, USA). qRT-PCR was performed with StepOnePlus™ Real-Time system (Applied Biosystems, USA) using PowerUp™ SYBR™ Green Master Mix. Fold expression was calculated as $2^{\Delta C_{tControl} - \Delta C_{tSample}}$. Human and mouse primer sequences, detailed in SI Table 1, were extracted from PrimerBank Database (https://pga.mgh.harvard.edu/primerbank/).

### 2.10. Extracellular flux analysis

Extracellular flux analysis assay was conducted in a Seahorse XFe24 flux analyzer (Agilent Technologies, USA). XFe24 sensor cartridges were calibrated overnight at 37 °C in Seahorse XF calibrant solution. Bioprinted muscle fibers were rinsed with Seahorse XF calibrant solution supplemented with 25 mM glucose and 2mM L-glutamine adjusted to pH 7.4. Rings were placed in the bottom of Seahorse XFe24 culture microplates and fixed for 15 min at 37 °C with 50 μl of Matrigel® (Corning Inc.). Fixed rings were rewashed and incubated for 1 h at 37 °C on supplemented Seahorse medium. For the metabolic flux assay, solutions of 5 μM Oligomycin, 0.5 μM FCCP and a mixture of 2 μM Antimycin and 1 μM Rotenone were prepared, all purchased from Sigma. To normalize data, analyzed rings were immersed in 100 μl extraction buffer [30 mM HEPES, 150 mM NaCl, pH 7.4, glycerol (10 % *v*/v), Triton X-100 (1 % v/v), sodium deoxycholate (DOC) (0.5 % *w/v*), complete Mini Protease Inhibitor Tablet (Roche, Switzerland) and PhosSTOP Phosphatase Inhibitor Tablet (Roche)]. Extracted samples were diluted 1:2, and total protein was quantified using Pierce™ BCA Protein Assay Kit (Thermo Fisher). All materials were purchased from Seahorse Bioscience (USA) unless specified.

### 2.11. Study of inflammatory factors

The inflammatory factors secreted by HCT116 and LS174T cell lines were determined using the Human Inflammation Array C2 from RayBiotech (USA), and TNFRI secretion in plasma of mice was analyzed using the Mouse sTNFRI ELISA Kit (RayBiotech) following the manufacture's protocol. Relative expression was calculated as the ratio of the factor spot intensity divided by the positive control intensity.

### 2.12. In vitro and in vivo models of cancer cachexia

*In vitro* models were developed using C2C12 monolayer (2D) and bioprinted muscle rings (3D). Differentiated fibers in both models were cultured in cancer cells-conditioned medium (CM) and control medium for 72 h. Control medium was obtained from C2C12 cells cultured at 80 % confluency for 48 h.

Male C57BL/6 J mice, 6–8 weeks old, were obtained from Charles River RMS Spain and used in this study. The Bioethical Committee of the Universidad Autónoma de Madrid and the competent authority approved the experimental protocol. All animal manipulations were made following the European Union guidelines. Mice were maintained on a regular dark-light cycle, with free access to food and water during the whole experimental period. After 2 weeks of adaptation to the local animal care facility, animals were randomly split into control inoculated mice and tumor-bearing mice.

### 2.13. Tumor cells inoculation

B16F10 melanoma cells were cultured in RPMI 1640 medium (Gibco) supplemented with 10 % fetal bovine serum (HyClone) and antibiotic (Lonza) at 37 °C and 5 % of $CO_2$. For inoculation, cells were removed from culture flasks by adding 0.05 % of trypsin solution, centrifuged, and re-suspended in sterile PBS to obtain a solution containing $1 \times 10^6$ cells/ml. Cell viability was determined by trypan blue exclusion. Finally, C57BL/6 J mice were subcutaneously injected with a solution of $5 \times 10^4$ cells in a final volume of 100 μl (50 μl of cell solution mixed with 50 μl of Matrigel- Corning), into the right flank. As a negative, control mice were inoculated with 50 μl of PBS mixed with 50 μl of Matrigel.

Animals were monitored at least three times a week for body weight, tumor dimensions, and health conditions and euthanized 24 days after tumor cells inoculation. On the day of sacrifice, blood was withdrawn from anesthetized mice (using sevoflurane) by cardiac puncture, collected in heparinized tubes, then centrifuged (1500 *g*, 10 min 4 °C) to obtain plasma. Quadriceps were rapidly excised and frozen in liquid nitrogen.

### 2.14. Statistical analysis

Data collected were presented as the mean ± standard deviation (SD) using GraphPad Prism software (GraphPad, USA). A *p*-value lower than 0.05 was considered statistically significant.

## 3. Results

### 3.1. Conditioning of GelMA-AlgMA bioinks for skeletal muscle tissue engineering

Hydrogels based on composite biomaterials present several advantages over single material formulations. Bioinks based on GelMA are highly printable and present different mechanical properties depending on the nature of the secondary component [19]. AlgMA improves the stability of hydrogels with encapsulated cells and reduces the degradation time. Nevertheless, the compressive modulus of GelMA-AlgMA hydrogels is lower than the stiffness of native skeletal muscle tissue. To obtain biomimetic hydrogels that mimic the stiffness of muscle tissue, we explored the effect of AlgMA concentration on the differentiation of muscle myoblasts. The stiffness of the photocrosslinked hydrogels was significantly affected by the concentration of AlgMA (Fig. 1a). Doubling the concentration of AlgMA to 2 % showed an increment in the compressive modulus from 1.57 to 20.32 kPa using a LAP concentration of 0.1 %, which better recapitulated the stiffness of the muscle. The effect of AlgMA concentration in muscle tissue development was evaluated by encapsulating muscle myoblasts in GelMA with 0 %, 1 % and 2 % of AlgMA. The staining of myosin heavy chain (MHC) and actin

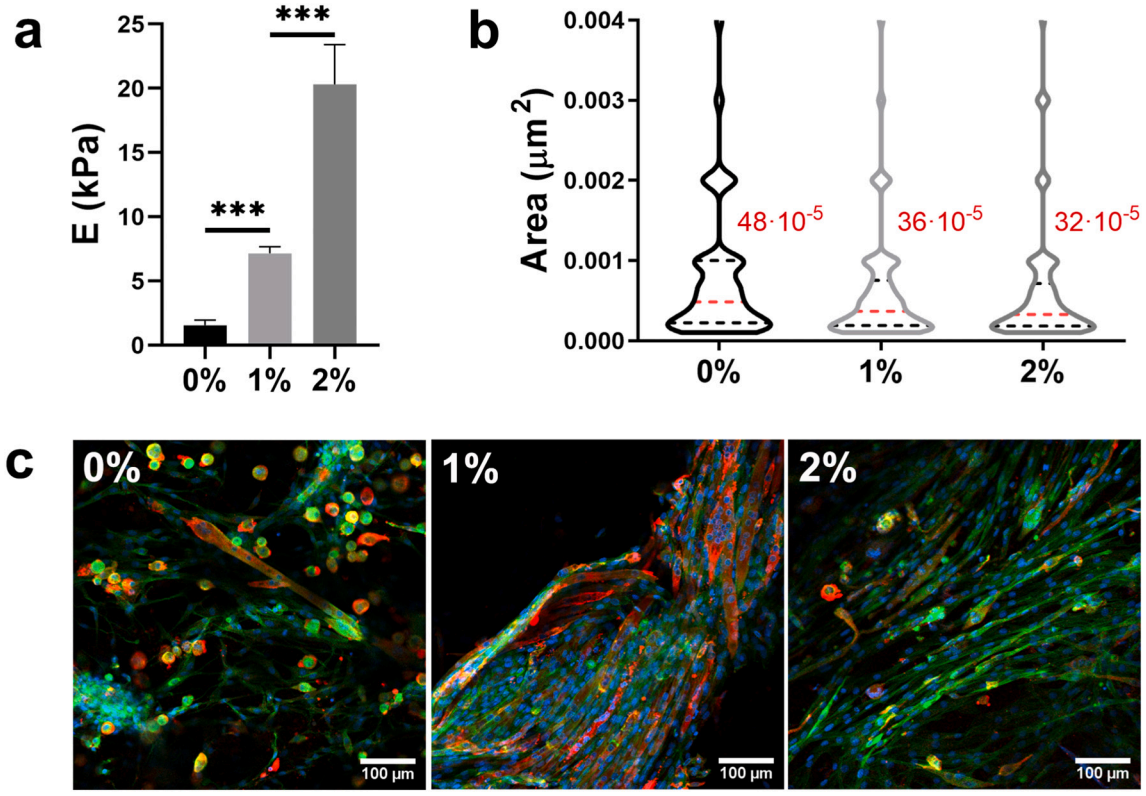


**Fig. 1.** Modulation of GelMA-AlgMA bioink mechanical properties. a) Compressive modulus E (kPa) of GelMA with 0 %,1 % and 2 % AlgMA ($n = 9$). b) Frequency distribution of the pore areas in the different GelMA-AlgMA formulations. Dashed black lines limit the interquartile region and the medians are presented as dashed red lines. c) Confocal images of C2C12 cells after 14 days of differentiation with stained MHC (red), F-actin (green) and nuclei (blue). Scale bar = 100 μm.

revealed a higher number of differentiated multinucleated myotubes in 1 % AlgMA. However, hydrogels with 2 % AlgMA presented thinner myotubes with a lower expression of MHC (Fig. 1b).

It is known that a high concentration of polymers in the precursor solution can result in crosslinked networks with closer pores [34]. Therefore, we measured the pore area of the different GelMA-AlgMA formulations (Fig. 1c). A higher concentration of AlgMA diminished the frequency of pores with higher areas, suggesting that the pore size influenced the differentiation of myoblasts. Matrices with small pores can hinder the migration and proliferation of cells [34,35], as well as affect the differentiation and growth of myotubes. At the sight of these results, we looked for an alternative strategy to obtain highly porous tissue-mimetic hydrogels. To keep the printability and differentiating nature of GelMA (5%*w/v*) – AlgMA (1%w/v) bioink, we explored the addition of a small amount of a third component, the fibrinogen (0.5% w/v) (Fig. 2a). The use of fibrinogen in skeletal muscle tissue engineering is extended due to its good myogenic properties [23,36]. It can be enzymatically crosslinked with thrombin, thus providing two strategies for modifying the physical properties when combined with GelMA-AlgMA: the dual crosslinking strategy [37] and modulating the photoinitiator concentration [38,39].

The printing fidelity of GelMA-AlgMA-Fibrin was calculated as the ratio of the spreading of the extruded filament and the needle diameter (Fig. 2a,b). Fibrin hydrogels showed a spreading ratio average of 2.4, which can be classified as a highly printable bioink in agreement with previous works [40]. The mean radius of printed filaments was 240 μm, which is inside the limits of nutrient diffusion established in gels [41]. Together, we confirmed the 0.02 % LAP/ GelMA-AlgMA-Fibrin bioink as the most suitable for fabricating 3D bioprinted muscle models.

SEM images of samples with the lowest LAP concentration revealed higher pore diameter (Fig. 2c). We observed a significant increase in materials' porosity when LAP concentration was reduced (Fig. 2d). The swelling analysis confirmed a greater availability of open pores in hydrogels with low LAP concentration (Fig. 2e). Concordantly, 0.01 % LAP hydrogels presented the highest maximum water absorbance, which increased from 60 % in 0.05 % LAP hydrogels to 150 %.

Then, we analyzed the resistance to hydrolysis and cell-derived collagenase (Fig. 2f). As expected, matrices with higher porosity enhanced the surface contact of polymer fibers, which increased 0.2 points the degradation rate. This effect was particularly notable in sample 0.01 % LAP samples, which showed fast degradation index and poor stability. LAP concentration has also a direct influence on the stiffness of photocrosslinked hydrogels (Fig. 2g). The reduction of LAP decreased the compressive modulus of hydrogels. Hydrogels with 0.05 % LAP presented 7.2 kPa. Concentrations of LAP above 0.05 % presented a lower stiffness, which was 2.5 times lower in 0.01 % LAP (2.8 kPa). LAP reduction improved the porosity of the hydrogels.

Fibrin aggregation increased the stiffness 2.9, 2.8 and 1.7-fold in 0.05 %, 0.02 % and 0.0.1 % LAP hydrogels respectively (Fig. 2g). The compressive modulus of hydrogels with 0.02 % LAP increased to 11.4 kPa, in the skeletal muscle tissue stiffness range (around 12 kPa). The degradation index indicated that fibrin also improved the hydrogel resistance to the enzymatic activity and hydrolysis, which was reduced by 0.2 points in 0.05 % and 0.02 % LAP hydrogels (Fig. 2f) and without a significant change in the porosity and swelling properties. (Figs. 2d,e).

Material's biocompatibility was compared by analyzing the circularity of encapsulated cells after 3 days in culture (Fig. 3a). Regardless of fibrin presence, hydrogels with 0.05 % LAP showed the highest content of circular cells, indicating lower cell adhesion and migration capability. The frequency of circular cells was reduced significantly when the concentration of LAP was diminished. Moreover, calcein staining revealed that fibrin addition did not compromise cell viability, which was very high (90 %) along with all the 3D cultures (Fig. 3b,c). The results evidenced that the porosity, swelling, degradation, and stiffness

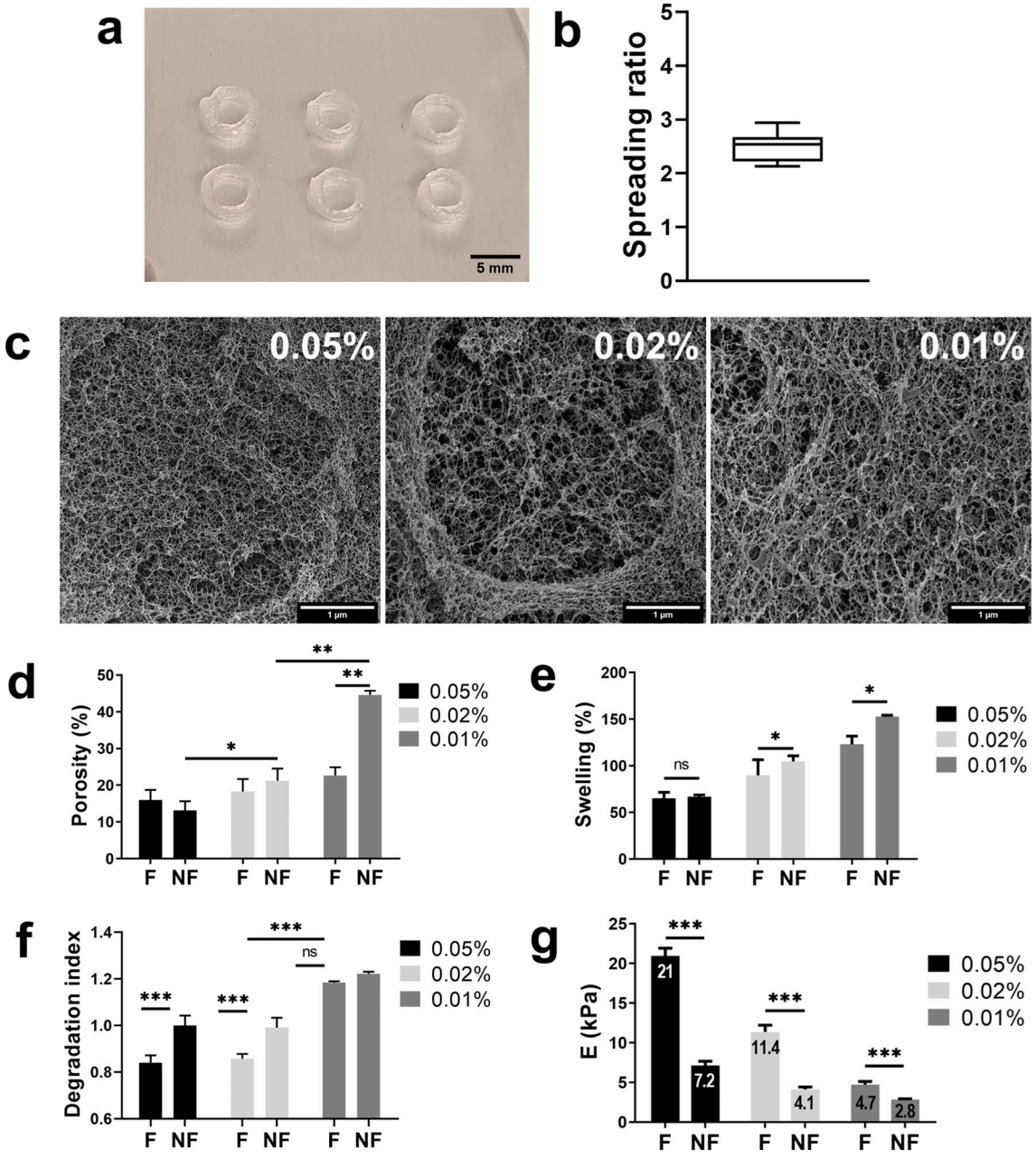


**Fig. 2.** Optimization of GelMA-AlgMA-based bioinks. a) Ring models of GelMA (5%*w/v*) – AlgMA (1 % w/v) – Fibrin (0.5%w/v) fabricated by extrusion bioprinting. b) Spreading ratio of GelMA-AlgMA-Fibrin extruded filaments. c) SEM images of GelMA-AlgMA biomaterials with 0.05 %, 0.02 % and 0.01 % w/v of LAP. Scale bar = 1 µm. Physical properties of the six GelMA-AlgMA biomaterials with (F) or without (NF) fibrin and 3 concentrations of LAP, including d) overall porosity (%) ($n$ = 3), e) swelling (%) ($n$ = 4), f) degradation index in collagenase (n = 4) and g) compressive modulus E (kPa) (n = 9). Data is presented as mean ± SD, two-way and one-way ANOVA *$p$-value <0.05, **p-value <0.005 and ***p-value <0.0005.

of 0.02 % LAP fibrin hydrogels improved the adhesion and viability of muscle myoblasts compared to other formulations with higher LAP content or without fibrin (Fig. 3c).

### 3.2. Establishment of a myogenic differentiation protocol for 3D bioprinted models

The design of 3D structures must be committed to mimicking the organization of the original tissue and facilitating the manipulation and life monitoring of samples. Ring models of 4.5 mm diameter and 1 mm height were designed to promote the concentric alignment of the myotubes and enable their immobilization around the pillar-like structure for life-imaging purposes (Fig. 4a,b). Myoblasts encapsulated in the photocrosslinked GelMA-AlgMA-Fibrin ring colonized the whole 3D structure, as shown in immunofluorescent images and paraffin sections (Fig. 4c,d). The actin cytoskeleton of cells was organized in parallel to the printing direction, confirming that extrusion bioprinting promoted the uniaxial alignment of cells (Fig. 4c).

Myoblasts were expanded in 3D for 8 days and then incubated in the differentiation medium (DM) or growth medium (GM) control. Confocal images revealed a poor density of fibers in the printed hydrogels after 7 days in DM (Fig. 5a). In contrast, models incubated in GM showed high fiber density in 3D cultures. Then, we analyzed cell proliferation to confirm the behavior of myoblasts during the growth and differentiation stages (Fig. 5b). The number of cells in DM cultures decreased after the medium change. This result could be associated with a higher death rate,

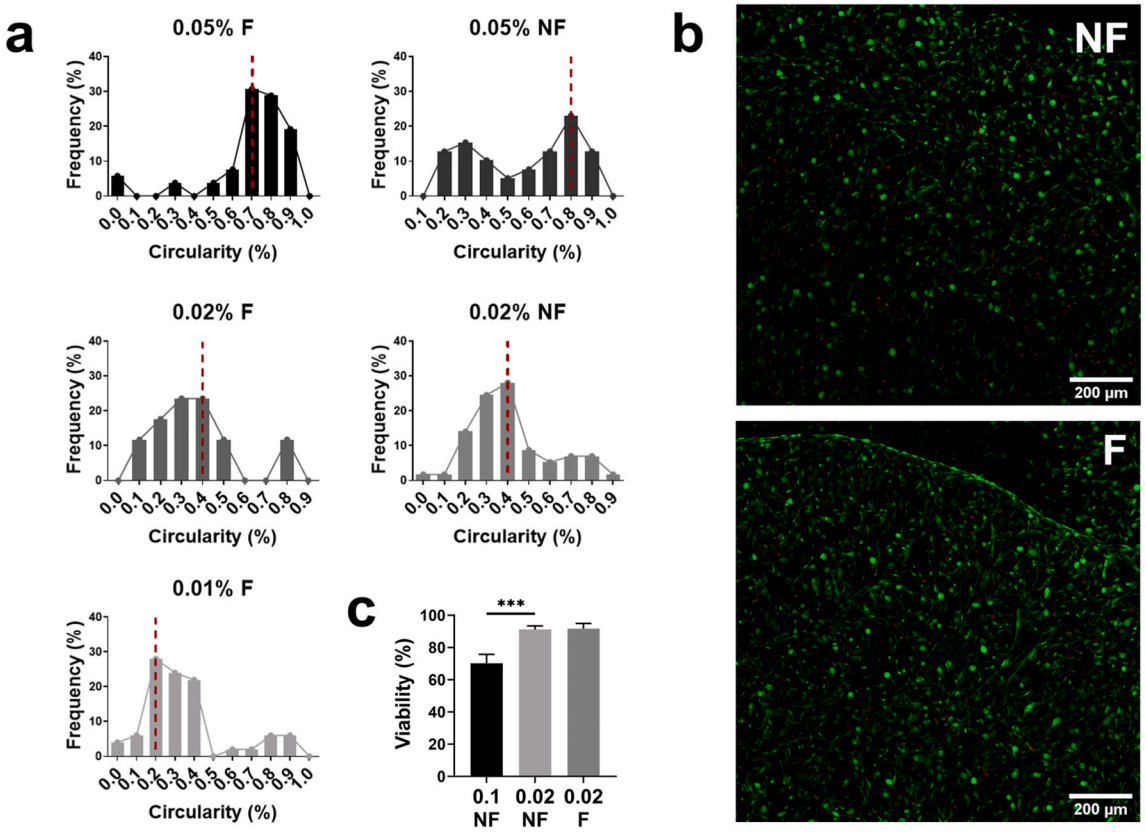


**Fig. 3.** Analysis of biocompatibility of GelMA-AlgMA hydrogels. a) Frequency (%) of cells with different circularity %. Circular cells are classified as 1 and tubular cells as 0. The median is represented as a red dashed line. b) Immunostaining of live (green) and dead (red) cells in 0.02 % LAP biomaterials after 3 days in culture. Scale bar = 200 µm. c) Viability of C2C12 after 3 days in culture in 0.02 % LAP biomaterial with (F) and without (NF) fibrin in comparison with the viability showed by previously developed biomaterial with 0.1 % LAP ($n = 5$). All 3D cultures were thicker than 100 µm. Data is presented as mean ± SD, two-way and one-way ANOVA *$p$-value <0.05, **p-value <0.005 and ***p-value <0.0005.

which agrees with the high number of round cells in confocal images.

Analyses of differentiation markers showed that DM did not significantly affect the expression of sarcomeric structural genes compared to GM (Fig. 5c). Confocal images of 3D models cultured in GM confirmed the expression of myosin heavy chain and α-actinin (two crucial proteins involved in myoblast differentiation) and the effect of the extrusion bioprinting process on the alignment of fibers towards the printing direction (Fig. 5d). The results suggested that the biomaterial presents myogenic activity, and DM would not be necessary to improve the differentiation. The quantification of the expression of myogenic regulatory factors (MRFs) (*Myf5, Myod1*, and *Myog*) and sarcomeric structural genes (*Actn2, Tnnc2, Myh4*, and *Myh7*) in myoblasts cultured in 2D and 3D in GM (Fig. 5e) shows in 2D cultures a high expression of MRFs and null expression of sarcomeric proteins. In contrast, 3D bioprinted models showed high expression of late differentiation genes, which confirm that the 3D biomaterial properties induce muscle differentiation.

### 3.3. Bioprinted human muscle models

For translatable purposes, we analyzed the behavior of Human Skeletal Muscle Myoblasts (HSMM) cultured within the same bioprinted rings in GM.

Live-dead analysis showed 80 % cell viability after 3 days of culture in 3D (Fig. 6a,b). Cell viability was lower than in mouse models. Most myoblasts showed elongated morphology, denoting good cell-ECM interaction that could encourage migration and proliferation. As expected, and in contrast to C2C12, HSMM maintained a constant cell number average over 15 days (Fig. 6c). Notably, MYF5 was downregulated, which indicates that myoblasts were committed to fiber differentiation. In concordance, intermediate differentiation (*MYOG*) and late differentiation genes (*ACTN2, MYH4*, and *MYH7*) were upregulated (Fig. 6d). Immunostaining images confirmed the expression of α-actinin and MHC (Fig. 6e), which revealed the formation of multinucleated fibers aligned towards the printing direction.

### 3.4. Addressing the functionality of bioprinted muscle models

First, the parameters for electrical stimulation were set up using a monolayer 2D model. We chose the lowest amplitude at which we obtained synchronous contraction (20 V) (Supplementary Video 1). The number of fibers contracting was significantly lower in samples stimulated with 10 V (Supplementary Video 2). The tetanic contraction was achieved when the pulse amplitude was set at 40 V (Supplementary Video 3). The number of contracting fibers subjected to 20 V, 2 ms, and 1 Hz pulses for 1 h increased after 3 days (Supplementary Fig. 1a). Cells showed upregulated expression of MHC and α-actinin (Supplementary Fig. 1b) after 3 days. Analysis of gene expression confirmed that α-actinin (*Actn2*) and one variant of MHC (*Myh7*) were also upregulated, while changes in *Tnnc2* and *Myh4* were not significant (Supplementary Fig. 1c).

For 3D bioprinted muscle rings submitted at the same electrical stimulation, the contraction amplitude of muscle fibers gradually increased during the 3 days of EPS (Fig. 7a) as observed for 2D culture. 3D bioprinted rings showed solid and synchronized contractions that accurately responded to different pulse frequencies (Fig. 7b), which showed fibers with a higher width than unstimulated fibers (Fig. 7c). In concordance with our previous work [32], differentiated fibers presented 70 % of fusion index, which was maintained in stimulated fibers

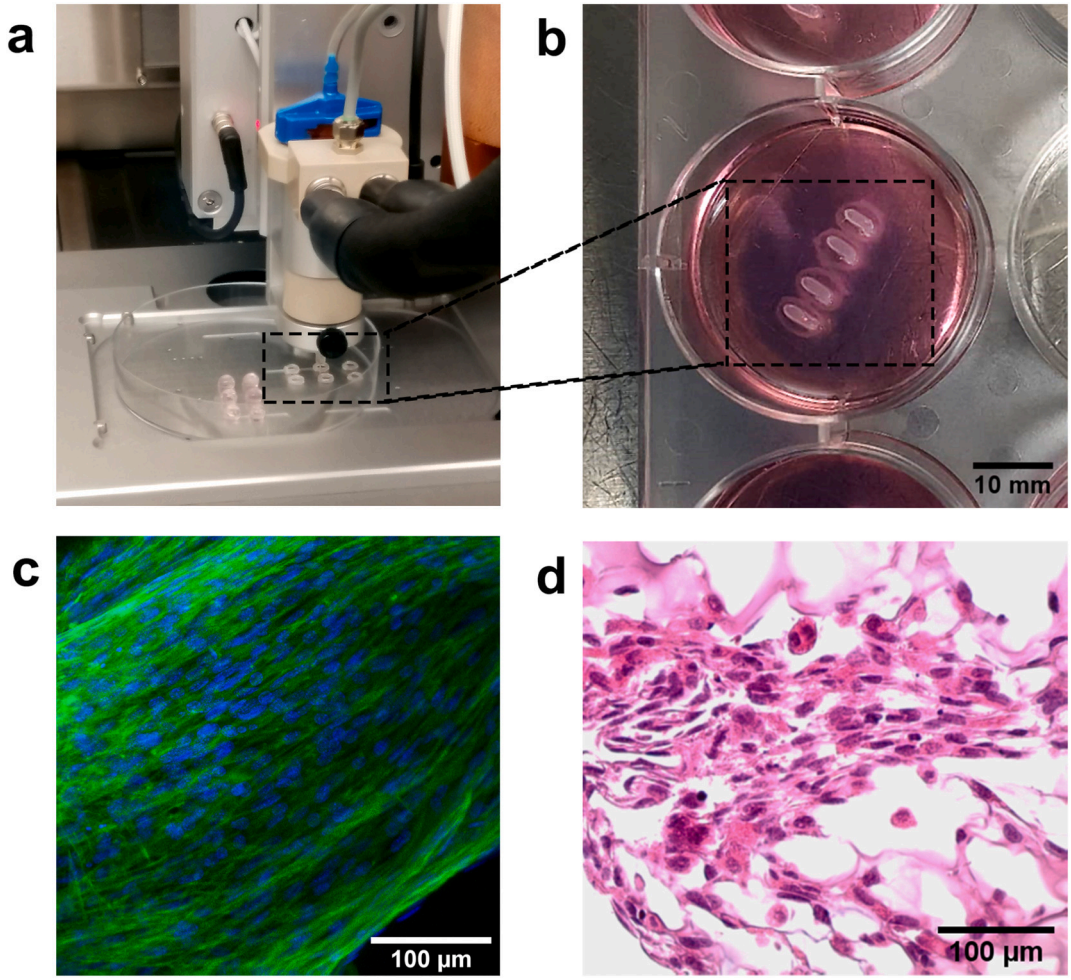


**Fig. 4.** Bioprinting of skeletal muscle models. a) Bioprinting process of ring models with encapsulated myoblasts. b) Muscle ring models anchored around 3D-printed silicon pillars. c) Immunofluorescence images of C2C12 myoblasts encapsulated in the bioprinted ring cultured for 7 days. F-actin is stained in green and nuclei in blue. Scale bar = 100 μm. d) Paraffined section of a bioprinted ring stained with hematoxylin-eosin. Scale bar = 100 μm.

(Fig. 7c). In contrast to stimulated monolayer cultures, gene expression analysis revealed that EPS did not significantly affect gene expression related to muscle differentiation (Fig. 7d). However, confocal images revealed an increase of multinucleated fibers with high expression of MHC and α-actinin. Furthermore, the actomyosin skeleton was organized into sharpening sarcomeres (Fig. 7e).

The extracellular metabolic flux of bioprinted rings was measured by the Seahorse XFe24 Flux Analyzer (Fig. 7f). The oxygen consumption rate of differentiated fibers after adding electron transport chain inhibitors (ETC) was measured. Encapsulated fibers finely responded to different inhibitors. Moreover, the response was immediate and proportional to the inhibitor dose, denoting that they were sensitive to changes in the medium composition.

### 3.5. Muscle wasting modeling induced by cancer cachexia

To explore the capability of bioprinted muscle rings to mimic better muscle wasting induced by cancer cachexia (CC) we choose colon cancer cell lines as well-known to induce CC. The presence of inflammatory factors related to CC in supernatants from two different colon cancer cell lines, HCT116 and LS174T were determined in the conditioned medium (CM) obtained from cell culture supernatants of cancer cells cultured in GM for 48 h. We found that LS174T cells secreted more inflammatory factors than HCT116 cells to the medium (Fig. 8a). Both cell lines presented significantly higher TNF receptor I (TNFRI) expression, showing LS174T with the highest expression. To confirm the relationship between TNFRI increase and cancer cachexia, we analyzed the concentration of TNFRI in the plasma of healthy and cachectic mice. We found that the concentration of TNFRI was 2-fold higher in cachectic mice compared with (Fig. 8b).

We next aimed to induce CC in 2D and 3D models by the treatment with CM for 72 h. Differentiated myotubes in 2D dramatically decreased fiber diameter (Fig. 8c, d). The morphology of fibers treated in 3D did not show noticeable changes between groups (Supplementary Fig. 2). Then, we evaluated the expression of genes related to CC in both models treated with CM compared to the quadriceps of mice with advanced cachexia. Gene expression of sarcomeric structural proteins, such as *Acnt2, Tnnc2, Myh4, Myh1*, and *Myh2*, was dramatically downregulated in the 2D systems, while we found minor changes in the expression of bioprinted muscles (Fig. 8e). In concordance with bioprinted muscles, *in vivo* analysis showed unaltered expression of sarcomeric proteins.

Notably, *Fbxo32/Atrogin1*, one of the essential E3 ubiquitin ligases in CC, was significantly upregulated in 3D and mice. Indeed, fold change over control was equitable in both models. In contrast, *Myh7* expression was upregulated in cachectic mice but not in 2D and 3D models. Bioprinted muscles showed upregulated expression of *Fbxo31*. However, neither 2D models nor cachectic mice presented expression changes. Lastly, *Fis1* was downregulated in 2D models, while the expression was unaltered in cachectic mice and 3D models showed significant upregulation.

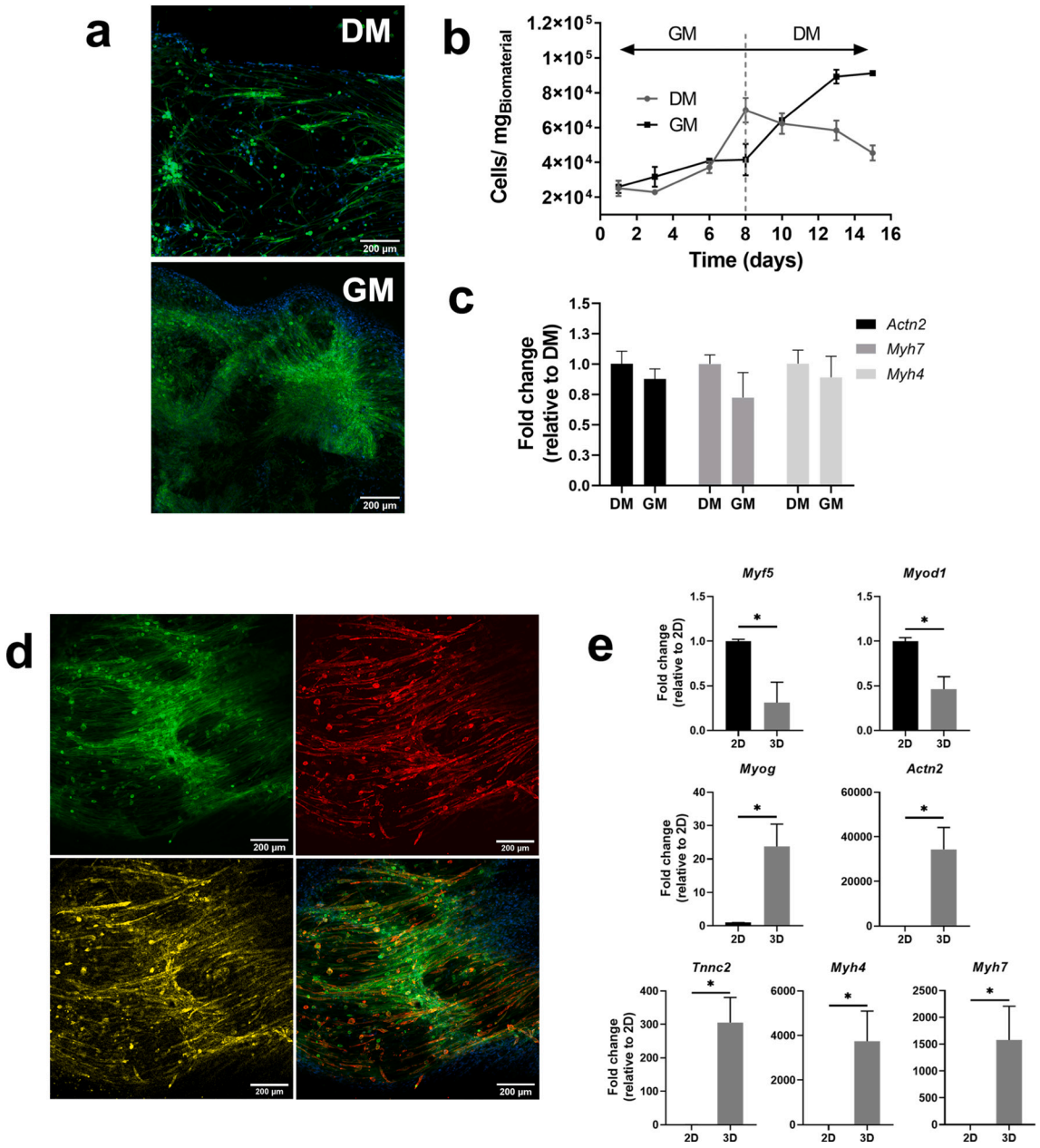


**Fig. 5.** Myogenic differentiation in 3D bioprinted models. a) Immunostaining of C2C12 cells after 15 days in bioprinted rings cultured in differentiation medium (DM) and growth medium (GM). Nuclei are stained in blue and green corresponds to F-actin ($n = 4$). Scale bar = 200 μm. b) proliferation of C2C12 cells in bioprinted rings cultured in DM and GM, calculated as number of cells per mg of biomaterial. c) mRNA expression of *Actn2, Myh7* and *Myh4* muscle differentiation genes in DM and GM cultures after 15 days (n = 4). d) Bioprinted rings after 15 days of culture in GM with differentiated fibers expressing α-actinin (yellow) and MHC (red). F-actin (green) and nuclei (blue) are also stained. Scale bar = 200 μm. e) Fold expression of myoblast stage (*Myf5* and *Myod1*), early differentiation stage (*Myog*) and late differentiation stage (*Actn2, Tnnc2, Myh4* and *Myh7*) genes in monolayer (2D) and bioprinted rings (3D) cultured in GM for 7 days (n = 4). Data is presented as mean ± SD, Unpaired *t*-test **p*-value <0.05, **p-value <0.005 and ***p-value <0.0005.

## 4. Discussion

Biomimetic materials that resemble the natural extracellular matrix are used to produce faithful skeletal muscle models. Mold-casted models are mostly manufactured with low viscous biomaterials with known myogenic properties, such as Matrigel, fibrin, and ECMs [22,42–44]. Myoblasts find excellent conditions to proliferate, migrate and fuse into mature muscle fibers. Bioprinting, instead, needs to find an equilibrium between the rheological properties of bioinks and the ensuing constraints in muscle tissue development. Nevertheless, the thixotropic properties of bioinks, together with the shear forces generated during extrusion printing, provides cylindric filaments formed by aligned polymer chains that can emulate the macro- and microstructure of skeletal muscle tissue [18]. In this work, we show the unidirectional alignment of myotubes without using passive tension forces generated by opposite pillars, as used in mold-casted models [22,42–44]. Bioprinting, as an additive manufacturing technique, provides automated production of tissue models, a fast modification of the model dimensions, the freedom to design complex 3D architectures, and easier scalability.

Bioinks can be achieved by the combination of different natural biomimetic materials. The intrinsic nature of each polymer provides a particular feature to the final mixture. This fact can be advantageous to meet the requirements of SMTE in terms of fabrication, mechanical

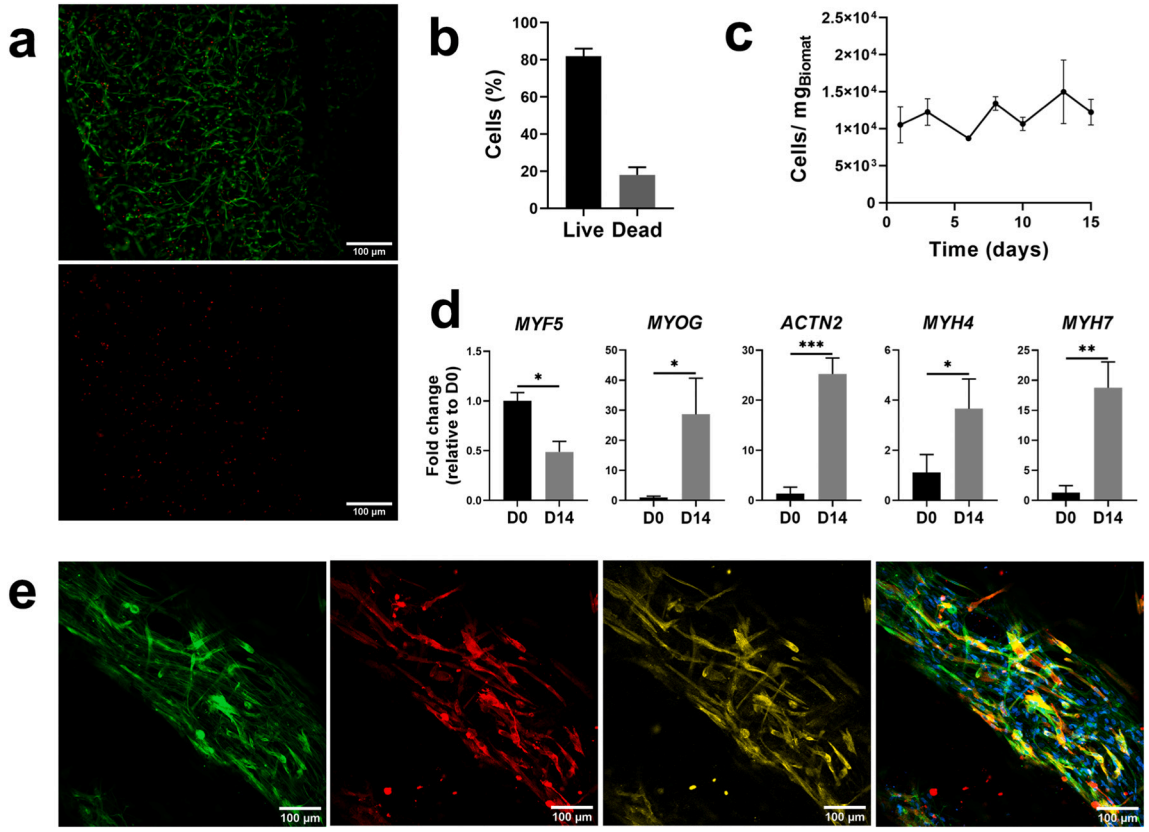


**Fig. 6.** Bioprinted muscle models. a) Staining of live (green) and dead (red) HSMM in GelMA-AlgMA-Fib bioprinted rings cultured for 3 days. Scale bar = 100 µm. HSMM b) viability after 3 days of culture and c) cell proliferation in bioprinted rings cultured for 15 days ($n = 13$). d) Analysis of expression of genes corresponding to myoblast stage (*MYF5*), early differentiation stage (*MYOG*) and late differentiation stage (*ACTN2, MYH4* and *MYH7*) by qRT-PCR in bioprinted rings cultured in HSMM growth medium for 14 days ($n = 5$). e) Immunostaining of bioprinted rings cultured for 14 days in GM showing HSMM fibers expressing MHC (red) and α-actinin (yellow). F-actin (green) and nuclei (blue) were also stained. Scale bar = 100 µm. Data is presented as mean ± SD, Unpaired *t*-test *$p$-value <0.05, **p-value <0.005 and ***p-value <0.0005.

properties, and biochemical signaling. Bioprinted muscle models have been fabricated using mixtures of gelatin and fibrinogen [36,45]. In this case, gelatin is used as a sacrificial material to improve the printability of the material. Constructs are enzymatically crosslinked after printing to ensure stability in culture conditions where gelatin is degraded. The resulting constructs are mainly based on pure fibrin, lacking the optimum mechanical properties for skeletal muscle tissue.

Furthermore, those natural polymers present high degradation rates that hinder the long-term stability of *in vitro* models. An alternative to achieve mechanically tunable hydrogels is based on photocrosslinkable materials. GelMA combines the high printability of gelatin and forms insoluble hydrogels suitable for cell culture. Furthermore, gelatin presents similar cell adhesion motifs to its precursor collagen [46].

We demonstrated that the combination of GelMA with AlgMA increased the resistance to degradation and stiffness of bioprinted hydrogels. To maintain the printability of the bioink, we preserved the concentration of GelMA and modified the concentration of AlgMA to achieve the mechanical properties of skeletal muscle tissue. However, a higher concentration of AlgMA negatively affected the differentiation of encapsulated myoblasts, which presented a lower density of myotubes with a smaller diameter and lower expression of the sarcomeric protein MHC. This effect is mainly due to the formation of polymer networks with low porosity resulting from an increased presence of monomers. Consequently, myoblast division and fusion are affected by matrix porosity. Additionally, matrices with small pores hamper the growth of myotubes [27,28].

The relevance of matrix porosity for muscle tissue development prompted us to develop hydrogels with improved porosity. Crosslinker concentration was modulated to improve the porosity of scaffolds and change the swelling of hydrogels [47,48]. We explored the limits of LAP concentration below 0.1 % using 0.05 %, 0.02 % and 0.01 %.

We found that the minimum photoinitiator concentration to obtain stable 3D cultures was 0.02 %. Lower LAP concentration resulted in higher pores, increasing the polymer surface exposure to the aqueous medium and cells. In line with those results, a decrease in LAP concentration dramatically reduced the compressive modulus of the hydrogels. Following our suspicions, cells encapsulated in 0.02 % LAP hydrogels showed higher viability and proliferation.

Nevertheless, the compressive modulus resulted in 4.1 kPa, below the stiffness of native muscle (12 kPa). Many works addressed the influence of matrix stiffness on the differentiation of precursor cells. Engler et al. showed that only those muscle fibers grown on surfaces mimicking muscle stiffness presented sarcomere structures [11]. Dual crosslinking of hydrogels based on UV light and the temperature has been applied to achieve structures with improved mechanical properties [36]. Fibrin addition significantly increased the compressive modulus of hydrogels, which reached 11.4 kPa, thus resembling the mechanical properties of muscle tissue. Furthermore, fibrin addition did not compromise the cell viability and biomaterial porosity and improved their resistance to degradation.

Differentiation of myoblasts is traditionally induced by serum starvation. A low concentration of growth factors guides their commitment to multinucleated myotubes [49,50]. Nevertheless, the treatment of myoblasts encapsulated in GelMA-AlgMA-Fibrin with the differentiation medium caused cell number reduction and muscle fibers degeneration. Distler et al. addressed that muscle cells encapsulated in ADA-GEL

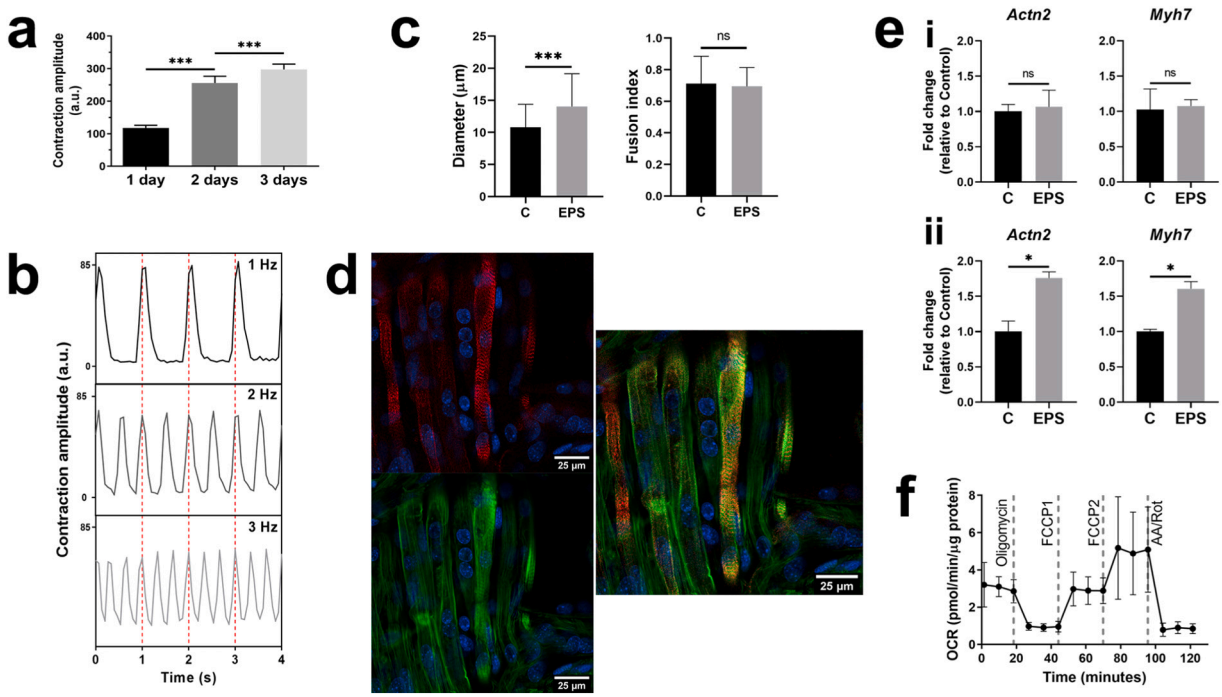


**Fig. 7.** EPS effect in bioprinted rings. a) Contraction amplitude of C2C12 fibers for 3 days of EPS ($n = 12$). Contraction amplitude data extracted from MUSCLE-MOTION and represented as arbitrary units. b) Electrograms of fiber contractions in 3D with different pulse frequencies (1 Hz, 2 Hz and 3 Hz). c) Muscle fiber diameter and fusion index of unstimulated (C) and stimulated bioprinted rings (EPS). d) qRT-PCR of differentiation genes in samples electrically stimulated for 3 days *vs* control ($n = 3$) in 3D models (i) and 2D bioprinted models (ii). e) Confocal images of C2C12 fibers treated with EPS for 3 days showing sarcomeric bands of F-actin (green) and α-actinin (yellow). MHC (red) and nuclei (blue) were also stained. Scale bar = 50 µm. f) Seahorse XFe24 extracellular flux profile showing the oxygen consumption rate normalized by µg of protein (OCR) after the application of ETC-targeting compounds. Data is presented as mean ± SD, one-way ANOVA and Unpaired *t*-test *$p$-value <0.05 and ***p-value <0.0005.

required high serum content to ensure the diffusion of nutrients inside 3D cultures [51]. We found high expression levels of sarcomeric proteins after 15 days in culture. Some studies reported that close cell-cell contact in highly dense cultures induces myoblast differentiation and growth arrest *via* CDKI p21 upregulation [52]. We wondered if differentiation commitment could be inhibited in low confluent cultures. Concordantly, we found high expression of myoblast stage genes in confluent monolayer cultures. However, cells in bioprinted rings significantly upregulated the expression of late differentiation stage genes despite the low confluency. The effect of matrix on the differentiation of muscle precursor cells was also visible in the human models. We found that HSMM encapsulated in GelMA-AlgMA-Fibrin and cultured in the growth medium for 15 days formed multinucleated fibers with high protein and gene expression of sarcomeric structural proteins.

Nevertheless, we found limited proliferation that resulted in a low number of encapsulated fibers. This result can be understood regarding the nature of immortalized C2C12 myoblasts, which possess unlimited proliferation. In contrast, HSMM primary cells are characterized by a limited proliferative capacity [53]. Together, these results revealed that GelMA-AlgMA-Fibrin bioink possessed myogenic properties and could induce the differentiation of muscle precursor cells. This effect could be related to the optimized biomaterial's mechanical properties and physical parameters. Nevertheless, fibrin could have an additional effect on the spontaneous differentiation of myoblasts. Thus, further studies should be performed to unveil the interaction between myoblasts and GelMA-AlgMA-Fibrin bioink.

Electrical stimulation of engineered muscles is an efficient method to address the functionality and maturation of the tissue. Bioprinted muscle models beated according to different frequencies and voltages. The electrical stimulation of rings led to slightly different results than the electrical stimulation of 2D cultures. After EPS treatment, bioprinted fibers displayed marked formation of sarcomeres and bigger myotubes, which agreed with the results obtained by Ito *et al* [54]. However, late differentiation genes were not significantly upregulated. During the EPS process, the contraction of fibers was strong, suggesting that cells in bioprinted rings achieved a more advanced maturation state before EPS treatment than in monolayer cultures. Therefore, a change in the expression of differentiation genes was not observed. However, the electrical stimulation notably accelerated the actomyosin rearrangement into sarcomeres and increased the width of fibers, which was indicative of a step forward in the maturation of the muscle model.

Oxygen basal consumption rate was similar to that in differentiated C2C12 monolayer cultures [55]. Basal consumption was more significant in single mouse fibers than C2C12 cultures [56]. The proliferative or differentiation state of cells can affect the oxidative activity of muscles. Still, it is also influenced by the muscle group, age, and culture conditions [55,57]. Commonly, OCR is normalized with the total protein content, which in our 3D models is significantly higher than in monolayer cultures due to the matrix composition. Regarding the changes in OCR rates because of different inhibitors during the Mito Stress analysis, the bioprinted fibers demonstrated high sensitivity to soluble extrinsic biomolecules, which modified the muscular metabolism similarly to single muscle fibers, as seen in the Seahorse analyzer. Altogether, the results highlighted the functionality and contractile activity of the bioprinted muscle.

The main application of our bioprinted muscle is focused on developing *in vitro* models of muscle wasting, as in cancer cachexia. The induction of muscle wasting using colorectal cancer cells conditioned medium (CM) showed that biomolecules in the media produced a strong and quick effect on the muscle fibers. After 72 h of treatment, we found that differentiated myotubes in 2D showed a shrunk morphology, downregulated expression of sarcomeric proteins, and slightly upregulated E3 ubiquitin ligases. *Myh7* encodes for the slow type myosin heavy chain, which is less vulnerable to the effects of cachexia than fast type

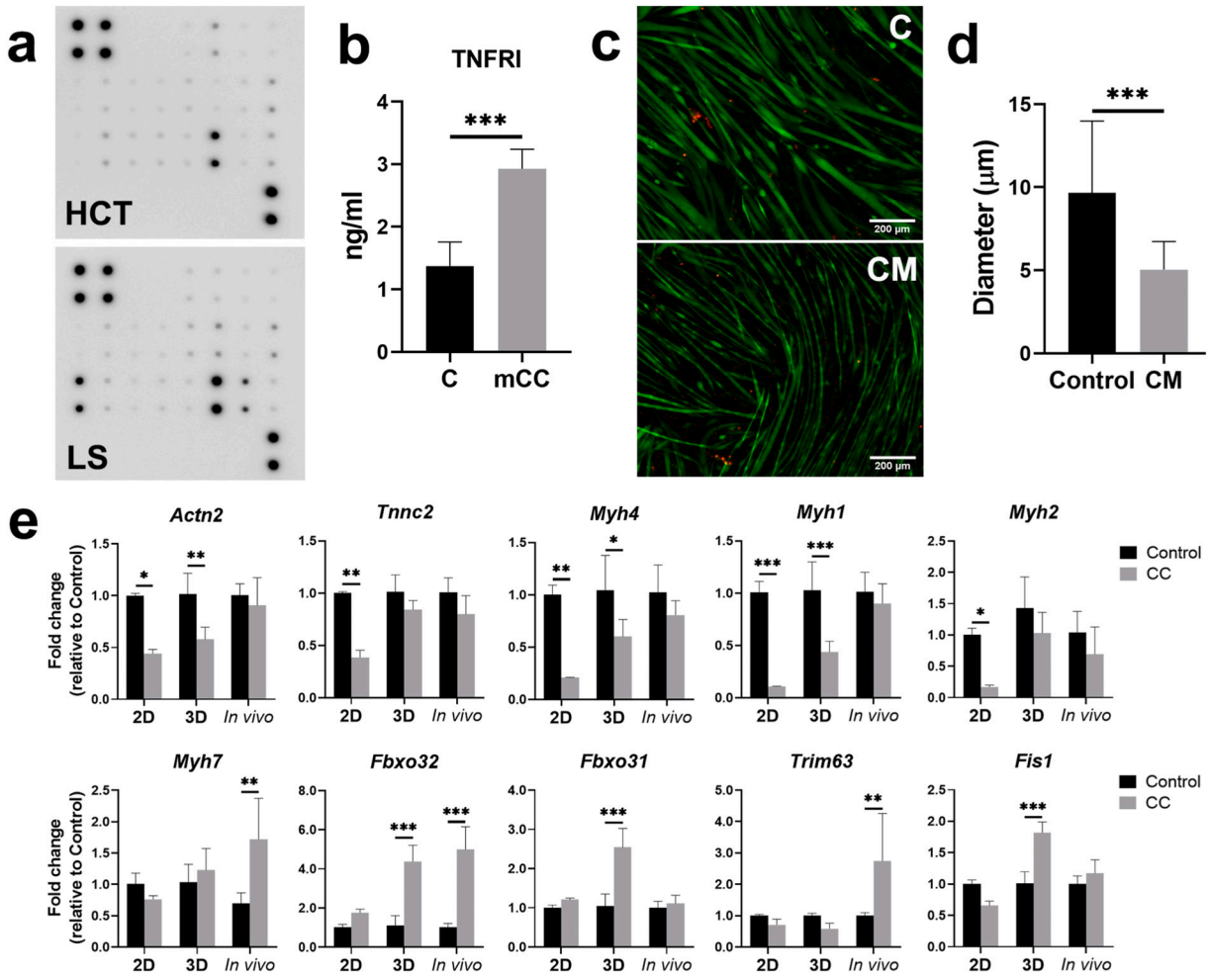


**Fig. 8.** Effect of colon cancer cell-conditioned medium (CM) in C2C12 monolayer culture and bioprinted rings. a) Array of inflammatory factors in HCT116 and LS174T CMs. b) TNFRI protein expression (ng·ml$^{-1}$) in plasma of control and cachectic mice (mCAQ) ($n = 4$). c) Confocal images of stained live (green) and dead (red) cells in control (C) and conditioned mediums (CM) for 72 h. Scale bar = 200 μm. d) Fiber diameter in CM and control medium after 72 h of treatment ($n = 42$). e) mRNA expression of fiber differentiation genes (*Actn2, Tnnc2, Myh4, Myh1, Myh2* and *Myh7*), E3-ubiquitin ligases (*Fbxo32, Trim 63* and *Fbxo31*) and autophagy related genes *(Fis1)* by qRT-PCR. Untreated (C) and cachexia models (CC) of monolayer cultures (2D), bioprinted rings (3D) and mice (*In vivo*) are shown (n = 4). Data is presented as mean ± SD, Unpaired t-test, One- and Two-way ANOVA *p-value <0.05, **p-value <0.005 and ***p-value <0.0005.

myosin [58,59]. In agreement with previous works, the expression of *Myh7* was not altered after CM treatment. This suggested that CM accelerated the protein degradation pathways and inhibited the synthesis pathways, which agrees with the phenotype and genotype of cachectic muscle found in the literature [59,60]. The presence of soluble inflammatory factors was evidenced in both conditioned media. The secretion of TNFα soluble receptor I (sTNFRI) was particularly relevant. High levels of sTNFRI in serum have been associated with late stages of CC and high mortality, thus suggesting TNFRI as a potential biomarker for CC [61]. Concordantly, we found a significantly higher level of sTNFRI in the plasma of tumor-bearing mice than in healthy individuals.

The treatment of the bioprinted model with CM unveiled some disparities between the 2D and 3D models. In contrast to 2D, fibers in the bioprinted model did not show apparent diameter reduction (Supplementary Fig. 2), and gene expression of sarcomeric proteins remained unchanged. Fiber morphology did not correspond to the phenotype of cachectic patients. However, we found that the gene expression was neither affected in cachectic mice. The results showed that the bioprinted model recapitulated the gene expression of cachectic mice better than monolayer cultures. Those similarities were confirmed after the study of ubiquitin ligases. While the upregulation of E3 ubiquitin ligases in 2D was almost negligible, the bioprinted model presented high *Fbxo32*, *Fbxo31*, and *Fis1*. The fold change of *Fbxo32* (Atrogin1) was comparable to that found in cachectic mice, which is known to be involved in the atrophy process induced by many types of cancer [60].

The upregulation of *Trim63* is commonly found in cachectic muscle tissue. However, we did not see expression changes in the bioprinted model. Many authors reported upregulated expression of *Trim63* in starvation conditions, which presented enhanced catabolic activity [62]. The controls were based on supernatants of C2C12 cultures to mask the effects of nutrient deprivation in the conditioned medium. The medium was incubated for 48 h, meaning the concentration of nutrients in the control medium was lower than in the complete fresh medium. We found that nutrient deprivation of the control medium significantly upregulated the expression of *Trim63* and *Fbxo31*, while *Fbxo32* was unaltered (Supplementary Fig. 3). The results suggest that *Trim63* had a more critical role in serum starvation, while *Fbxo32* was essential for muscle atrophy in CC of the *in vitro* models.

## 5. Conclusions

We developed a 3D skeletal muscle model using bioprinting techniques for muscle wasting studies The fabrication of printed ring models made easy-handling models anchored in pillar-like structures for further experiments. In contrast to other fabrication techniques, such as mold casting, the fabrication of skeletal muscle models is fast and automated

and does not require further manipulation steps after printing. The bioink formulation was optimized to mimic the physical properties of skeletal muscle tissue. The combination of the rheological properties of GelMA, which provided a highly printable bioink, with AlgMA, which increased the resistance to degradation, resulted in hydrogels suitable for long-lasting *in vitro* experiments. Additionally, fibrin provided an accurate control of the crosslinking process that notably increased the compressive modulus of hydrogels without compromising the porosity and printability. GelMA-AlgMA-Fibrin biomaterial crosslinked with 0.02 % LAP presents a higher pore diameter than previous formulations, mimics the stiffness of native muscle, and exhibits myogenic activity that triggers the differentiation of human and mouse myoblasts. Bioprinted muscle recapitulated the structure, functionality, gene expression, and metabolic behavior of native muscle more faithfully.

The 3D bioprinted models treated with colorectal cancer cells conditioned medium showed upregulation of E3 ubiquitin ligases. In particular, *Fbxo 32 (Atrogin 1)* expression in 3D was comparable to that found in the cachectic mice, which is known to be involved in the atrophy process induced by many types of cancer. The bioprinted tissue recapitulated better some features seen in the skeletal muscle of patients suffering from cancer cachexia than the standard 2D muscular models used for drug screening. Therefore, we propose our bioprinted muscle model as a more predictive, non-costly, and feasible platform to study muscle diseases as muscle wasting.

Supplementary data to this article can be found online at https://doi.org/10.1016/j.bioadv.2023.213426.

## CRediT authorship contribution statement

AGL performed experiments, analyzed and interpreted the results, and wrote the manuscript; AV supervised the study, interpreted the results, and wrote the manuscript; JAL, MF, MCS, DS and LH performed experiments; JS supervised the study, interpreted the results and wrote the manuscript.

## Declaration of competing interest

The authors declare that they have no competing interests.

## Data availability

Data will be made available on request.

## Acknowledgments

This work is supported by the Project BASE3D funded by the Tecnologies Emergents programme of the General Directorate for Research – Generalitat de Catalunya (ref. 001-P-001646) and co-funded by the European Regional Development Fund (ERDF) Operational Program of Catalonia 2014-2020 with a grant of 50 % of total cost eligible. The IBEC Group was supported by the Networking Biomedical Research Center (CIBER), Spain. CIBER is an initiative funded by the VI National R&D&i Plan 2008–2011, Iniciativa Ingenio 2010, Consolider Program, CIBER Actions, and the Instituto de Salud Carlos III (RD16/0006/0012), with the support of the European Regional Development Fund (ERDF). This work was funded by the CERCA Programme and by the Commission for Universities and Research of the Department of Innovation, Universities, and Enterprise of the Generalitat de Catalunya (2021 SGR 01545). This work has been developed in the context of AdvanceCat with the support of ACCIÓ (Catalonia Trade and Investment; Generalitat de Catalunya) under the Catalonian ERDF operational program 2014–2020. AV is supported by the Spanish Association Against Cancer (AECC), and the R+D+ i grant "Research challenges" (RTI) PID2020-117977RA-I00.

This work was also supported by project PI 19/0142, from the Instituto de Salud Carlos III (Ministry of Economy, Industry and Competitiveness) and cofunded by the European Regional Development Fund, and approved by the Ethics Committee of our Institution.

This study was supported by the Ministry of Spain (MINECO) (SAF2017-83813-C3-1-R to DS and LH cofunded by the ERDF, the Centro de Investigación Biomédica en Red de Fisiopatología de la Obesidad y la Nutrición (CIBEROBN) (Grant CB06/03/0001 to DS), the Government of Catalonia (2017SGR278 to DS), and the Fundació La Marató de TV3 (201627-30 to DS).

## References

[1] S.M. Abmayr, G.K. Pavlath, Myoblast fusion: lessons from flies and mice, Development 139 (2012) 641–656, https://doi.org/10.1242/dev.068353.
[2] J.M. Argilés, S. Busquets, B. Stemmler, F.J. López-Soriano, Cancer cachexia: Understanding the molecular basis, Nature Reviews Cancer 14 (11) (2014) 754–762, https://doi.org/10.1038/nrc3829. Nature Publishing Group.
[3] G.P. Marceca, P. Londhe, F. Calore, Management of cancer cachexia: attempting to develop new pharmacological agents for new effective therapeutic options, in: Frontiers in Oncology, Vol. 10, Frontiers Media S.A, 2020, p. 298, https://doi.org/10.3389/fonc.2020.00298.
[4] M. Bove, A. Carlucci, G. Natale, C. Freda, A. Noro, V. Ferrara, G. Opromolla, M. Martone, R. Cascone, G. Messina, A. Izzo, G. Vicidomini, M. Santini, A. Fiorelli, Tissue engineering in musculoskeletal tissue: a review of the literature, Surgeries 2 (2021) 58–82, https://doi.org/10.3390/surgeries2010005.
[5] S.K. Shukla, A. Dasgupta, K. Mehla, V. Gunda, E. Vernucci, J. Souchek, G. Goode, R. King, A. Mishra, I. Rai, S. Nagarajan, N.V. Chaika, F. Yu, P.K. Singh, Silibinin-mediated metabolic reprogramming attenuates pancreatic cancer-induced cachexia and tumor growth, Oncotarget 6 (38) (2015) 41146–41161, https://doi.org/10.18632/oncotarget.5843.
[6] G. Zhang, Z. Liu, H. Ding, H. Miao, J.M. Garcia, Y.P. Li, Toll-like receptor 4 mediates Lewis lung carcinoma-induced muscle wasting via coordinate activation of protein degradation pathways, Sci. Rep. 7 (1) (2017), https://doi.org/10.1038/s41598-017-02347-2.
[7] J. Yang, Z. Zhang, Y. Zhang, X. Ni, G. Zhang, X. Cui, M. Liu, C. Xu, Q. Zhang, H. Zhu, J. Yan, V.F. Zhu, Y. Luo, J.P. Hagan, Z. Li, J. Fang, A. Jatoi, M. E. Fernandez-Zapico, L. Zheng, M. Li, ZIP4 promotes muscle wasting and cachexia in mice with orthotopic pancreatic tumors by stimulating RAB27B-regulated release of extracellular vesicles from cancer cells, Gastroenterology 156 (3) (2019) 722–734, https://doi.org/10.1053/j.gastro.2018.10.026, e6.
[8] K. Shimizu, R. Genma, Y. Gotou, S. Nagasaka, H. Honda, Three-dimensional culture model of skeletal muscle tissue with atrophy induced by dexamethasone, Bioengineering 4 (2) (2017), https://doi.org/10.3390/bioengineering4020056.
[9] M. Menconi, P. Gonnella, V. Petkova, S. Lecker, P.O. Hasselgren, Dexamethasone and corticosterone induce similar, but not identical, muscle wasting responses in cultured L6 and C2C12 myotubes, J. Cell. Biochem. 105 (2) (2008) 353–364, https://doi.org/10.1002/jcb.21833.
[10] E. Archer-Lahlou, C. Lan, R.T. Jagoe, Physiological culture conditions alter myotube morphology and responses to atrophy treatments: implications for in vitro research on muscle wasting, Physiol. Rep. 6 (12) (2018), https://doi.org/10.14814/phy2.13726.
[11] A.J. Engler, S. Sen, H.L. Sweeney, D.E. Discher, Matrix elasticity directs stem cell lineage specification, Cell 126 (2006) 677–689, https://doi.org/10.1016/j.cell.2006.06.044.
[12] N. Jiwlawat, E.M. Lynch, B.N. Napiwocki, A. Stempien, R.S. Ashton, T.J. Kamp, W. C. Crone, M. Suzuki, Micropatterned substrates with physiological stiffness promote cell maturation and pompe disease phenotype in human induced pluripotent stem cell-derived skeletal myocytes, Biotechnol. Bioeng. 116 (2019) 2377–2392, https://doi.org/10.1002/bit.27075.
[13] D. Neal, M.S. Sakar, L.-L.S. Ong, H.H. Asada, Lab on a Chip Formation of Elongated Fascicle-inspired 3D Tissues Consisting of High-density, Aligned Cells Using Sacrificial Outer Molding 14, 2014, https://doi.org/10.1039/c4lc00023d.
[14] M. Samandari, J. Quint, A. Rodríguez-delaRosa, I. Sinha, O. Pourquié, A. Tamayol, Bioinks and bioprinting strategies for skeletal muscle tissue engineering, Adv. Mater. 34 (12) (2022) 2105883, https://doi.org/10.1002/ADMA.202105883.
[15] A.J. Capel, R.P. Rimington, J.W. Fleming, D.J. Player, L.A. Baker, M.C. Turner, J. M. Jones, N.R.W. Martin, R.A. Ferguson, V.C. Mudera, M.P. Lewis, Scalable 3D printed molds for human tissue engineered skeletal muscle, Front. Bioeng. Biotechnol. 7 (FEB) (2019) 20, https://doi.org/10.3389/fbioe.2019.00020.
[16] P. Heher, B. Maleiner, J. Prüller, A.H. Teuschl, J. Kollmitzer, X. Monforte, S. Wolbank, H. Redl, D. Rünzler, C. Fuchs, A novel bioreactor for the generation of highly aligned 3D skeletal muscle-like constructs through orientation of fibrin via application of static strain, Acta Biomater. 24 (2015) 251–265, https://doi.org/10.1016/j.actbio.2015.06.033.
[17] S.G.M. Uzel, R.J. Platt, V. Subramanian, T.M. Pearl, C.J. Rowlands, V. Chan, L. A. Boyer, P.T.C. So, R.D. Kamm, Microfluidic device for the formation of optically excitable, three-dimensional, compartmentalized motor units, Sci. Adv. 2 (8) (2016), e1501429, https://doi.org/10.1126/sciadv.1501429.
[18] P. Mozetic, S.M. Giannitelli, M. Gori, M. Trombetta, A. Rainer, Engineering muscle cell alignment through 3D bioprinting, J. Biomed. Mater. Res. Part A 105 (2017) 2582–2588, https://doi.org/10.1002/jbm.a.36117.
[19] W.J. Kim, G.H. Kim, 3D bioprinting of functional cell-laden bioinks and its application for cell-alignment and maturation, Appl. Mater. Today 19 (2020), 100588, https://doi.org/10.1016/j.apmt.2020.100588.

[20] M. Samandari, J. Quint, A. Rodríguez-delaRosa, I. Sinha, O. Pourquié, A. Tamayol, Bioinks and bioprinting strategies for skeletal muscle tissue engineering, Adv. Mater. 34 (12) (2022) 2105883, https://doi.org/10.1002/ADMA.202105883.
[21] S.W. Sawyer, K. Takeda, A. Alayoubi, E. Mirdamadi, A. Zidan, S.R. Bauer, H. Degheidy, 3D bioprinting optimization of human mesenchymal stromal cell laden gelatin-alginate-collagen bioink, Biomed. Mater. 18 (1) (2022), 015016, https://doi.org/10.1088/1748-605X/ACA3E7.
[22] A.Alave Reyes-Furrer, S.De Andrade, D. Bachmann, H. Jeker, M. Steinmann, N. Accart, A. Dunbar, M. Rausch, E. Bono, M. Rimann, H. Keller, Matrigel 3D bioprinting of contractile human skeletal muscle models recapitulating exercise and pharmacological responses, Commun. Biol. 41 (4) (2021) 1–12, https://doi.org/10.1038/s42003-021-02691-0.
[23] H.-W. Kang, S.J. Lee, I.K. Ko, C. Kengla, J.J. Yoo, A. Atala, A 3D bioprinting system to produce human-scale tissue constructs with structural integrity, Nat. Biotechnol. 34 (2016) 312–319, https://doi.org/10.1038/nbt.3413.
[24] C. O'Connell, J. Ren, L. Pope, Y. Li, A. Mohandas, R. Blanchard, S. Duchi, C. Onofrillo, Characterizing bioinks for extrusion bioprinting: printability and rheology, Methods Mol. Biol. 2140 (2020) 111–133, https://doi.org/10.1007/978-1-0716-0520-2_7.
[25] A.C. Daly, S.E. Critchley, E.M. Rencsok, D.J. Kelly, A comparison of different bioinks for 3D bioprinting of fibrocartilage and hyaline cartilage, Biofabrication 8 (2016), 045002, https://doi.org/10.1088/1758-5090/8/4/045002.
[26] R. Seyedmahmoud, B. Çelebi-Saltik, N. Barros, R. Nasiri, E. Banton, A. Shamloo, N. Ashammakhi, M.R. Dokmeci, S. Ahadian, Three-dimensional bioprinting of functional skeletal muscle tissue using gelatin methacryloyl-alginate bioinks, Micromachines 10 (2019) 679, https://doi.org/10.3390/MI10100679.
[27] K. Wolf, M. te Lindert, M. Krause, S. Alexander, J. te Riet, A.L. Willis, R. M. Hoffman, C.G. Figdor, S.J. Weiss, P. Friedl, Physical limits of cell migration: control by ECM space and nuclear deformation and tuning by proteolysis and traction force, J. Cell Biol. 201 (7) (2013) 1069, https://doi.org/10.1083/JCB.201210152.
[28] S. Jana, A. Cooper, M. Zhang, S. Jana, A. Cooper, M. Zhang, Chitosan scaffolds with unidirectional microtubular pores for large skeletal myotube generation, Adv. Healthcare Mater. 2 (4) (2013) 557–561, https://doi.org/10.1002/ADHM.201200177.
[29] M.E. Prendergast, M.D. Davidson, J.A. Burdick, G. Janarthanan, J. Hyun Kim, I. Kim, E. Fornetti, F. De Paolis, C. Fuoco, S. Bernardini, S.M. Giannitelli, A. Rainer, D. Seliktar, F. Magdinier, J. Baldi, R. Biagini, S. Cannata, S. Testa, C. Gargioli, A novel extrusion-based 3D bioprinting system for skeletal muscle tissue engineering, Biofabrication 15 (2) (2023) 025009, https://doi.org/10.1088/1758-5090/ACB573.
[30] S.Y. Sonaye, E.G. Ertugral, C.R. Kothapalli, P. Sikder, Extrusion 3D (bio)printing of alginate-gelatin-based composite scaffolds for skeletal muscle tissue engineering, Materials 15 (22) (2022) 7945, https://doi.org/10.3390/MA15227945.
[31] M. Costantini, S. Testa, P. Mozetic, A. Barbetta, C. Fuoco, E. Fornetti, F. Tamiro, S. Bernardini, J. Jaroszewicz, W. Święszkowski, M. Trombetta, L. Castagnoli, D. Seliktar, P. Garstecki, G. Cesareni, S. Cannata, A. Rainer, C. Gargioli, Microfluidic-enhanced 3D bioprinting of aligned myoblast-laden hydrogels leads to functionally organized myofibers in vitro and in vivo, Biomaterials 131 (2017) 98–110, https://doi.org/10.1016/j.biomaterials.2017.03.026.
[32] A. García-Lizarribar, X. Fernández-Garibay, F. Velasco-Mallorquí, A.G. Castaño, J. Samitier, J. Ramon-Azcon, Composite biomaterials as long-lasting scaffolds for 3D bioprinting of highly aligned muscle tissue, Macromol. Biosci. (2018) 1800167, https://doi.org/10.1002/mabi.201800167.
[33] L. Sala, B.J. van Meer, et al., MUSCLEMOTION: a versatile open software tool to quantify cardiomyocyte and cardiac muscle contraction in vitro and in vivo, Circ. Res. (2017), https://doi.org/10.1161/CIRCRESAHA.117.312067.
[34] J. Vandaele, B. Louis, K. Liu, R. Camacho, P.H.J. Kouwer, S. Rocha, Structural characterization of fibrous synthetic hydrogels using fluorescence microscopy, Soft Matter 16 (17) (2020) 4210–4219, https://doi.org/10.1039/C9SM01828J.
[35] S.M. Lien, L.Y. Ko, T.J. Huang, Effect of pore size on ECM secretion and cell growth in gelatin scaffold for articular cartilage tissue engineering, Acta Biomater. 5 (2) (2009) 670–679, https://doi.org/10.1016/J.ACTBIO.2008.09.020.
[36] J.H. Kim, I. Kim, Y.J. Seol, I.K. Ko, J.J. Yoo, A. Atala, S.J. Lee, Neural cell integration into 3D bioprinted skeletal muscle constructs accelerates restoration of muscle function, Nat. Commun. 11 (2020) 1–12, https://doi.org/10.1038/s41467-020-14930-9.
[37] N.S. Kajave, T. Schmitt, T.U. Nguyen, V. Kishore, Dual crosslinking strategy to generate mechanically viable cell-laden printable constructs using methacrylated collagen bioinks, Mater. Sci. Eng. C 107 (2020), 110290, https://doi.org/10.1016/J.MSEC.2019.110290.
[38] H. Chavda, C. Patel, Effect of crosslinker concentration on characteristics of superporous hydrogel, Int. J. Pharm. Investig. 1 (1) (2011) 17, https://doi.org/10.4103/2230-973X.76724.
[39] K. Kabiri, H. Omidian, S.A. Hashemi, M.J. Zohuriaan-Mehr, Synthesis of fast-swelling superabsorbent hydrogels: effect of crosslinker type and concentration on porosity and absorption rate, Eur. Polym. J. 39 (7) (2003) 1341–1348, https://doi.org/10.1016/S0014-3057(02)00391-9.
[40] J. Nulty, F.E. Freeman, D.C. Browe, R. Burdis, D.P. Ahern, P. Pitacco, Y. Bin Lee, E. Alsberg, D.J. Kelly, 3D bioprinting of prevascularised implants for the repair of critically-sized bone defects, Acta Biomater. 126 (2021) 154–169, https://doi.org/10.1016/J.ACTBIO.2021.03.003.
[41] L. Corstorphine, M.V. Sefton, Effectiveness factor and diffusion limitations in collagen gel modules containing HepG2 cells, J. Tissue Eng. Regen. Med. 5 (2) (2011) 119–129, https://doi.org/10.1002/TERM.296.
[42] L. Madden, M. Juhas, W.E. Kraus, G.A. Truskey, N. Bursac, Bioengineered human myobundles mimic clinical responses of skeletal muscle to drugs, elife 2015 (2015), https://doi.org/10.7554/ELIFE.04885.
[43] C. Vesga-Castro, J. Aldazabal, A. Vallejo-Illarramendi, J. Paredes, Contractile force assessment methods for in vitro skeletal muscle tissues, elife 11 (2022), https://doi.org/10.7554/ELIFE.77204.
[44] A.D. Hofemeier, T. Limon, T.M. Muenker, B. Wallmeyer, A. Jurado, M.E. Afshar, M. Ebrahimi, R. Tsukanov, N. Oleksiievets, J. Enderlein, P.M. Gilbert, T. Betz, Global and local tension measurements in biomimetic skeletal muscle tissues reveals early mechanical homeostasis, elife 10 (2021) 1–27, https://doi.org/10.7554/ELIFE.60145.
[45] T. Fan, S. Wang, Z. Jiang, S. Ji, W. Cao, W. Liu, Y. Ji, Y. Li, N. Shyh-Chang, Q. Gu, Controllable assembly of skeletal muscle-like bundles through 3D bioprinting, Biofabrication 14 (1) (2021), 015009, https://doi.org/10.1088/1758-5090/AC3ACA.
[46] N. Davidenko, C.F. Schuster, D.V. Bax, R.W. Farndale, S. Hamaia, S.M. Best, R. E. Cameron, Evaluation of cell binding to collagen and gelatin: a study of the effect of 2D and 3D architecture and surface chemistry, J. Mater. Sci. Mater. Med. 27 (10) (2016) 148, https://doi.org/10.1007/S10856-016-5763-9.
[47] H. Chavda, C. Patel, Effect of crosslinker concentration on characteristics of superporous hydrogel, Int. J. Pharm.Investig. 1 (1) (2011) 17, https://doi.org/10.4103/2230-973X.76724.
[48] K. Kabiri, H. Omidian, S.A. Hashemi, M.J. Zohuriaan-Mehr, Synthesis of fast-swelling superabsorbent hydrogels: effect of crosslinker type and concentration on porosity and absorption rate, Eur. Polym. J. 39 (7) (2003) 1341–1348, https://doi.org/10.1016/S0014-3057(02)00391-9.
[49] S.M. Maffioletti, S. Sarcar, A.B.H. Henderson, I. Mannhardt, L. Pinton, L.A. Moyle, H. Steele-Stallard, O. Cappellari, K.E. Wells, G. Ferrari, J.S. Mitchell, G.E. Tyzack, V.N. Kotiadis, M. Khedr, M. Ragazzi, W. Wang, M.R. Duchen, R. Patani, P. S. Zammit, D.J. Wells, T. Eschenhagen, F.S. Tedesco, Three-dimensional human iPSC-derived artificial skeletal muscles model muscular dystrophies and enable multilineage tissue engineering, Cell Rep. 23 (2018) 899–908, https://doi.org/10.1016/j.celrep.2018.03.091.
[50] D. Gholobova, M. Gerard, L. Decroix, L. Desender, N. Callewaert, P. Annaert, L. Thorrez, Human tissue-engineered skeletal muscle: a novel 3D in vitro model for drug disposition and toxicity after intramuscular injection, Sci. Rep. 8 (2018) 1–14, https://doi.org/10.1038/s41598-018-30123-3.
[51] T. Distler, A.A. Solisito, D. Schneidereit, O. Friedrich, R. Detsch, A.R. Boccaccini, 3D printed oxidized alginate-gelatin bioink provides guidance for C2C12 muscle precursor cell orientation and differentiation via shear stress during bioprinting, Biofabrication 12 (2020), 045005, https://doi.org/10.1088/1758-5090/ab98e4.
[52] K. Tanaka, K. Sato, T. Yoshida, T. Fukuda, K. Hanamura, N. Kojima, T. Shirao, T. Yanagawa, H. Watanabe, Evidence for cell density affecting C2C12 myogenesis: possible regulation of myogenesis by cell-cell communication, Muscle Nerve 44 (2011) 968–977, https://doi.org/10.1002/mus.22224.
[53] A. Skardal, Bioprinting essentials of cell and protein viability, in: Essentials 3D Biofabrication Transl, Elsevier Inc., 2015, pp. 1–17, https://doi.org/10.1016/B978-0-12-800972-7.00001-3.
[54] A. Ito, Y. Yamamoto, M. Sato, K. Ikeda, M. Yamamoto, H. Fujita, E. Nagamori, Y. Kawabe, M. Kamihira, Induction of functional tissue-engineered skeletal muscle constructs by defined electrical stimulation, Sci. Rep. 4 (2015) 4781, https://doi.org/10.1038/srep04781.
[55] A.M. Abdelmoez, L.S. Puig, J.A.B. Smith, B.M. Gabriel, M. Savikj, L. Dollet, A. V. Chibalin, A. Krook, J.R. Zierath, N.J. Pillon, Comparative profiling of skeletal muscle models reveals heterogeneity of transcriptome and metabolism, Am. J. Physiol. Cell Physiol. 318 (2020) 615–626, https://doi.org/10.1152/ajpcell.00540.2019.-Rat.
[56] H. Lee, T.Y. Ha, C.H. Jung, F.S. Nirmala, S.Y. Park, Y.H. Huh, J. Ahn, Mitochondrial dysfunction in skeletal muscle contributes to the development of acute insulin resistance in mice, J. Cachexia. Sarcopenia Muscle 12 (2021) 1925–1939, https://doi.org/10.1002/JCSM.12794.
[57] F. Pala, D. Di Girolamo, S. Mella, S. Yennek, L. Chatre, M. Ricchetti, S. Tajbakhsh, Distinct metabolic states govern skeletal muscle stem cell fates during prenatal and postnatal myogenesis, J. Cell Sci. 131 (2018), https://doi.org/10.1242/JCS.212977/56828.
[58] S. Ciciliot, A.C. Rossi, K.A. Dyar, B. Blaauw, S. Schiaffino, Muscle type and fiber type specificity in muscle wasting, Int. J. Biochem. Cell Biol. 45 (2013) 2191–2199, https://doi.org/10.1016/j.biocel.2013.05.016.
[59] N. Johns, S. Hatakeyama, N.A. Stephens, M. Degen, S. Degen, W. Frieauff, C. Lambert, J.A. Ross, R. Roubenoff, D.J. Glass, C. Jacobi, K.C.H. Fearon, Clinical classification of cancer cachexia: phenotypic correlates in human skeletal muscle, PLoS One 9 (2014), e83618, https://doi.org/10.1371/journal.pone.0083618.
[60] G. Wang, A.K. Biswas, W. Ma, M. Kandpal, C. Coker, P.M. Grandgenett, M. A. Hollingsworth, R. Jain, K. Tanji, S. López-Pintado, A. Borczuk, D. Hebert, S. Jenkitkasemwong, S. Hojyo, R.V. Davuluri, M.D. Knutson, T. Fukada, S. Acharyya, Metastatic cancers promote cachexia through ZIP14 upregulation in skeletal muscle, Nat. Med. 24 (2018) 770–781, https://doi.org/10.1038/s41591-018-0054-2.
[61] D. Aderka, H. Engelmann, V. Hornik, Y. Skornick, Y. Levo, D. Wallach, G. Kushtai, Increased serum levels of soluble receptors for tumor necrosis factor in cancer patients, Cancer Res. 51 (20) (1991).
[62] R. Sartori, V. Romanello, M. Sandri, Mechanisms of muscle atrophy and hypertrophy: implications in health and disease, Nature Communications 12 (1) (2021) 1–12, https://doi.org/10.1038/s41467-020-20123-1.